Available on CMS information server

CMS NOTE 2003/017

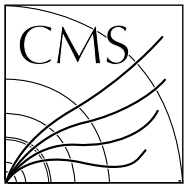

The Compact Muon Solenoid Experiment

CMS Note

Mailing address: CMS CERN, CH-1211 GENEVA 23, Switzerland

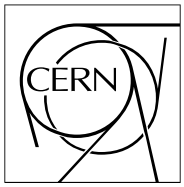

TEST OF MB3 MUON BARREL DRIFT CHAMBERS WITH COSMIC RAYS

F. R. Cavallo

INFN sez. Bologna, V.le Berti Pichat 6/2, Bologna, Italy

M. Benettoni, E. Conti, M. De Giorgi, F. Gasparini, U. Gasparini, F. Gonella, A. T. Meneguzzo, F. Montecassiano, M. Passaseo, M. Pegoraro, P. Ronchese, E. Torassa, S. Vanini, G. Zumerle

INFN sez. Padova, Via Marzolo 8, Padova, Italy

Abstract

Production of the muon barrel drift chambers called MB3 for the CMS experiment at the LHC has started at Legnaro INFN Labs in 2001. The detectors are fully equipped with the final front-end electronics and high-voltage boards, and test pulse and low-voltage systems. Before being moved to CERN, all chambers are tested and validated. After good noise level and proper high voltage behavior have been ensured, we collect cosmic-ray events triggered by an external scintillator system. We use those data to infer the main parameters of the chambers, namely, detection efficiency, uniformity in behavior, timing properties (resolution, uniformity, dependence on track angle), and possible shifts of the wires and layers inside the superlayers. The method is particularly efficient in finding pathologies caused by trivial mistakes like, for example, an unconnected electrode, which can be quickly recovered.

1 Introduction

The CMS barrel muon detection system [1] consists of 4 concentric shells of wire drift chambers, called MB1 (the innermost), MB2, MB3, and MB4 (the outermost). Each chamber (except the MB4 type) is made of 3 independent units, called SuperLayers (SL), and a thick honeycomb plate glued together, as shown in fig. 1. Each SL is composed of 4 layers of drift tubes, with all wires parallel. The wires of odd layers inside a SL are staggered by a half-cell width with respect to the even layers. The two external SLs, called $\Phi 1$ and $\Phi 2$, have wires in the same direction and measure the muon trajectory in the CMS bending plane. The third SL, called Θ, has wires perpendicular to the Φ SLs. The drift tube, with $43 \times 13\ mm^2$ cross section, shown schematically in fig. 2, is composed of three electrodes: a wire, where the electron multiplication occurs, two I-beams (cathodes), and two strips, which define the electric drift field and provide some shaping to it, thus improving its uniformity. For MB3 chambers, the wire length is $237.9\ cm$ and $302.1\ cm$ for Φ and Θ SLs, respectively. Each Φ SL contains 286 channels, each Θ SL 227 channels, for a total of 799 channels/chamber.

Production of MB3 chambers [1, 2, 3] for the CMS muon barrel began in 2001 at the Legnaro INFN Laboratories. Before being glued together, each of the 3 SLs are checked one by one to guarantee gas tightness, a minimum electronic noise level and good high voltage behavior. A detailed description of such tests and of their results can be found in ref. [4]. After being assembled and before being moved to CERN, all chambers are further tested to check the electronic noise rate, detection efficiency, uniformity of behavior, time resolution, and wire, layer and SL position. The chambers are built using the final design [1, 2, 3] and equipped with the final front-end electronics, final high-voltage boards, and final high-voltage and low-voltage internal layout and cables. Only the TDCs and the data acquisition system are not the ones foreseen for CMS, but are temporary solutions developed for local tests and test beams.

All measurements are performed by using cosmic rays crossing the chamber and triggered by a system of plastic scintillators. After the cosmic-ray events are collected (1 million events in a couple of hours), data analysis is performed and we can quickly identify and localize wrong features of the chamber, as discussed below, and try to fix them. This fine-grain and fast testing procedure is repeated until a fully-efficient and well-performing chamber is obtained. Particularly relevant are the measurements of the wire, layer and superlayer positions and the check that systematic shifts were not introduced in the construction phase. In fact, while correction of the nominal position of the wires can be applied in the offline analysis to improve spatial resolution, the online first-level trigger [5] requires that the tolerances are fulfilled at the construction level. Safe values of tolerances are 0.1 mm for the wire position inside the SL and 1 mm for the relative position of the SLs. Should systematic shifts occur, a proper correction to the assembly procedure has to be applied.

The purpose of this note is to present the testing procedure and the analysis in order to demonstrate the reliability and efficiency of the diagnostic method.

Besides the routine analysis for validating the chamber, other studies have been performed to understand the effect of different incidence angles of the incoming tracks, the after-pulse rate and its dependence on wire gain and detection threshold, and the drift velocity dependence on the absolute gas pressure. Some of these will be presented here. All data presented here refer to the same chamber (except when stated otherwise), MB3-011, which behaved typically.

2 Experimental setup and procedure

After the chamber is glued, it is placed horizontally on a table and filled with an Ar(85%)-CO_2(15%) gas mixture. The oxygen concentration [O_2] is measured by an oxygen monitor [1)] placed downstream just before the gas exhaust. As soon as [O_2] $\approx 200\ ppm$, the gas flow is reduced and regulated in such a way that the absolute pressure is kept constant. Typically $P = 1020\ mbar$ and the gas flow is $0.2\ l/min$, corresponding to about a full gas exchange every 3 days. The *standard* high voltage values of the cell electrodes are: $V_{wire} = 3700\ V$, $V_{strip} = 1800\ V$, and $V_{I-beam} = -1200\ V$. At these voltages, the wire gain is on the order of $3 \div 5 \cdot 10^5$ [6] which is about the same value as in our previous runs at CERN ([7, 8, 9, 10]).

The front-end electronics (FE) is composed of a fast charge preamplifier ($33\ ns$ integration time) followed by a shaper (shaping time of $15\ ns$) and a discriminator [11]. The *standard* discriminator threshold is $15\ mV$, which corresponds to a charge of about $4.5\ fC$.

Signals from the chamber front-end electronics are fed into 18 TDCs [2)] set in common stop mode. The TDCs have

[1)] Zirconia oxygen analyzer series 350, by Panametrics.

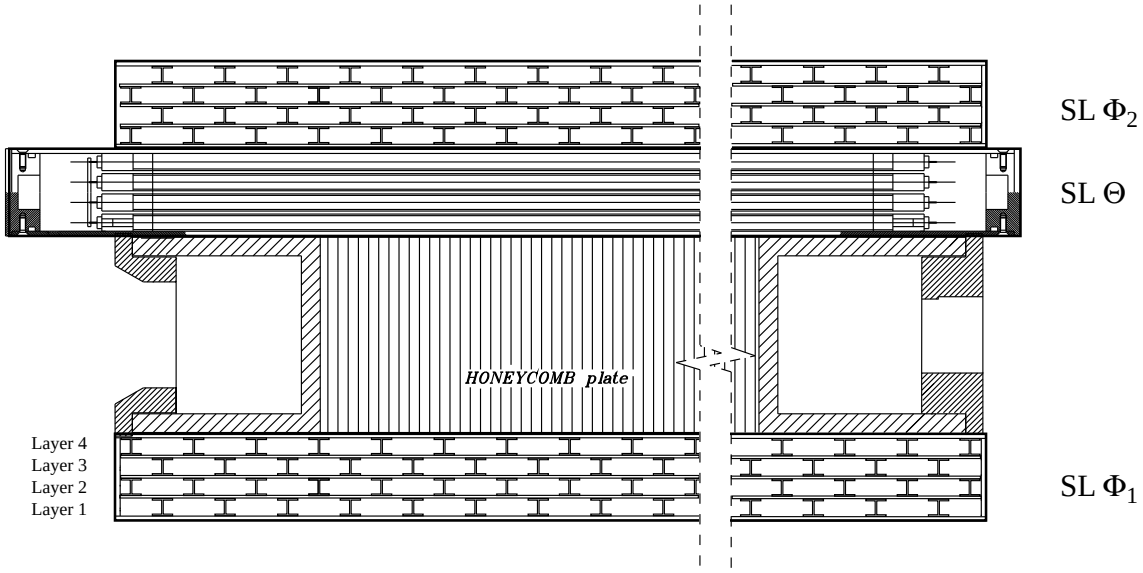

Figure 1: A cross section through an MB3 chamber.

a clock of 96 kHz. The DAQ system, which reads out the TDCs and stores the data, and the online monitor are described in detail in [12].

Under the table, a system of plastic scintillators detects cosmic rays crossing the chamber, and gives the trigger and the common stop time to the TDCs. The trigger efficiency is about 75% and the trigger rate is about $180\ Hz$, allowing us to collect 10^6 events in two hours. For each trigger, the hits occurred within a time window of $32\ \mu s$ are recorded and stored.

Since the number of available TDC channels is not enough to read-out the entire chamber in a single run, we have to collect the data in two runs: i) the entire Θ plus the left half of $\Phi 1$ and $\Phi 2$, and ii) the entire Θ plus the right half of $\Phi 1$ and $\Phi 2$.

2.1 Cosmic-ray trigger

8 plastic scintillators, arranged in 4 pairs of overlapping elements, provide the cosmic-ray trigger (fig. 3). The two pairs composed of the longest scintillators ($300 \times 20\ cm^2$ area, $2\ cm$ thick) are placed parallel to the Θ wires (therefore perpendicular to the Φ wires), about 90 cm underneath the table plane. The other two groups, composed of $250 \times 27\ cm^2$ area, $2\ cm$ thick scintillators, are placed perpendicular to the Θ wires, $50\ cm$ underneath the table plane. A block scheme of the trigger logic is sketched in fig. 4. Each scintillator is readout at the two ends by two photomultipliers (PMTs) [3)]. After discrimination, the two signals from the PMTs are fed into a mean-timer module [14], which yields the mean time of the two signals. Then the two mean times of each pair are put in coincidence. The cosmic-ray trigger is given by the logical OR of the AND of each pair.

The plastic scintillators are quite old and have been extensively exploited by other experiments. Consequently, their intrinsic light-emission properties are degraded, resulting in a poor time resolution for the trigger (several ns). Therefore, this trigger is not adequate to study the time resolution of the chamber (see also fig. 19). The synchronization of the 4 pairs of scintillators has been performed by triggering them with a small plastic scintillator with a time resolution better than $1\ ns$ which provides the reference time.

3 Test of Front-End electronics

Before starting to collect cosmic-ray tracks, we perform a check of the electronic noise rate and measure the delay time caused by the cable lengths, channel by channel.

[2)] 32-channel VME TDC board, developed at INFN Roma for the KLOE experiment [13].

[3)] Thorn EMI model 9813KB.

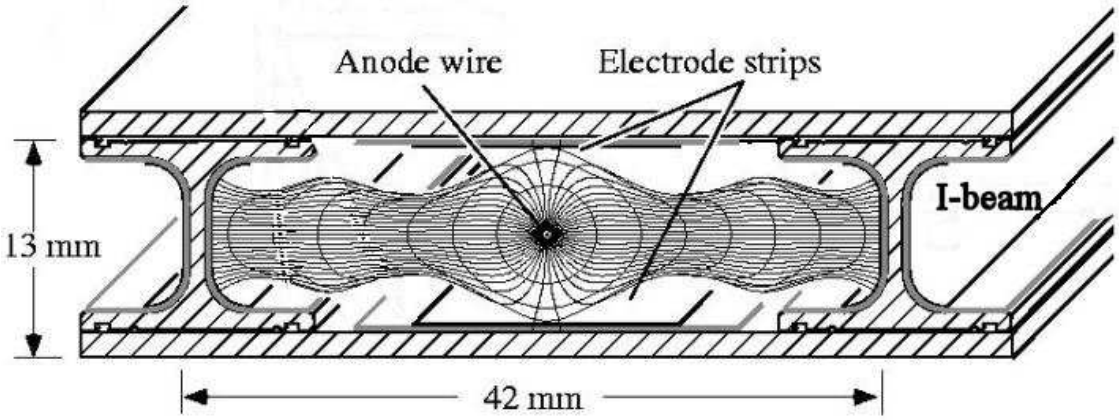

Figure 2: A schematic view of a drift tube. The drift lines which reach the wire are also shown.

A test pulse signal is provided to each channel's front-end amplifier and the delay time $t_{0,i}$ between the test pulse and the output signal is measured, channel by channel (index i). $t_{0,i}$ depends not only on the cable length, but also on the front-end discriminator threshold level. To have an idea of the risetime of the front-end output signal, we measured the variation of the delay time with the threshold by looking at signals from cosmic rays (and not from test pulses). Figure 5 shows the measured dependence of $t_{0,i}$ on the threshold value V_{thr}, where the delay at $V_{thr} = 10\ mV$ has been put arbitrarily to zero. The risetime is well below 10 ns.

For the analysis of the data, the hit drift times t_i are corrected for the delay time $t_{0,i}$.

With the chamber at the nominal HV value, random triggers are provided by a pulser. The number of hits inside the time window and the window width determine the noise rate of a cell. As an example, fig. 6 shows the noise rate, channel by channel, for all layers of chamber MB3-011. The average noise rate as a function of the threshold value is plotted in fig. 7. The Θ SL are systematically noisier than the Φ SL because of the longer wire length. At the standard threshold value of $15\ mV$ and standard HV conditions, the average noise rate is around $40 - 50\ Hz$/channel for the Φ SL and around $60\ Hz$/channel for the Θ SL, both rates corresponding to a *linear noise density* of about 0.2 Hz/cm of wire.

At a threshold of $15\ mV$, we also measure the average noise rate as a function of V_{wire}. The result is shown in fig. 8.

4 Test with cosmic rays: Efficiency

The measurement of the chamber efficiency is not performed using the external cosmic-ray trigger because of varying geometric acceptance, but relies on the reconstruction of cosmic-ray track segments in each superlayer.

Each recorded drift time, after subtraction of the individual delay time, is converted into two positions (due to the left-right ambiguity) assuming a constant drift velocity v_{drift} ($55\ \mu m/ns$) (see [8, 10] and sect.5). The reconstruction of a track segment requires hits in at least three different layers inside a SL. Then all possible combinations of points are fitted to a straight line and the best fit is chosen. The track is accepted if the fit fulfills the condition $\chi^2 \leq 100$ (using in the fit a single wire resolution of $300\ \mu m$). We apply such a loose cut to avoid possible bias introduced by the event selection. We verified that the track finding efficiency is not affected by variation of v_{drift} within 5% .

We measure the layer efficiency, the cell efficiency and the efficiency dependence on the position inside the cell. For all cases, we look for tracks with at least three hits in different layers and check if a fourth hit is present in the fourth layer within a fixed window L ($4.2\ cm$) around the track extrapolation.

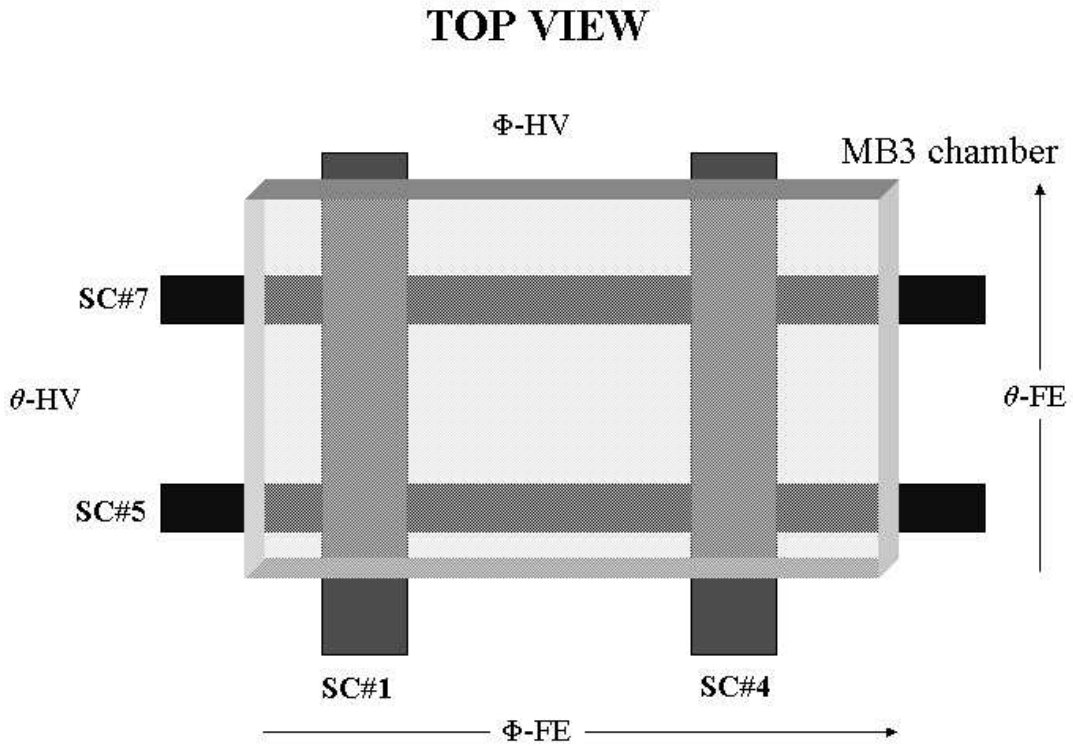

Figure 3: A schematic of the scintillator layout for the cosmic-ray trigger. *FE* and *HV* label the front-end and the high voltage side of the SL, respectively. The arrow directions reflect the numbering of the FE channels (origin corresponds to channel 1)

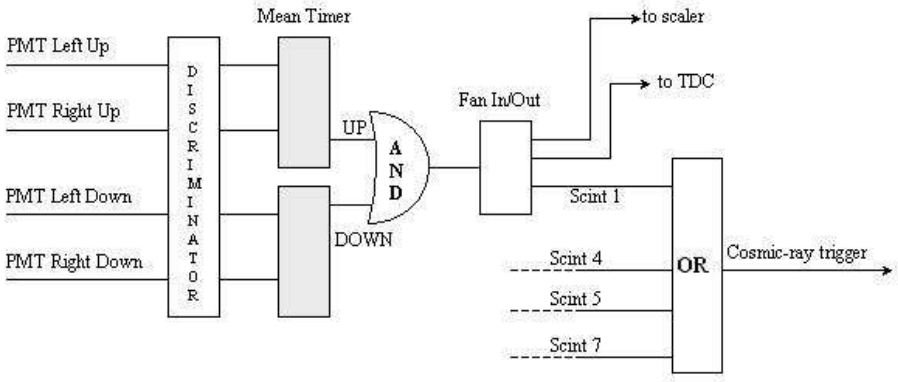

Figure 4: A schematic of the trigger logic.

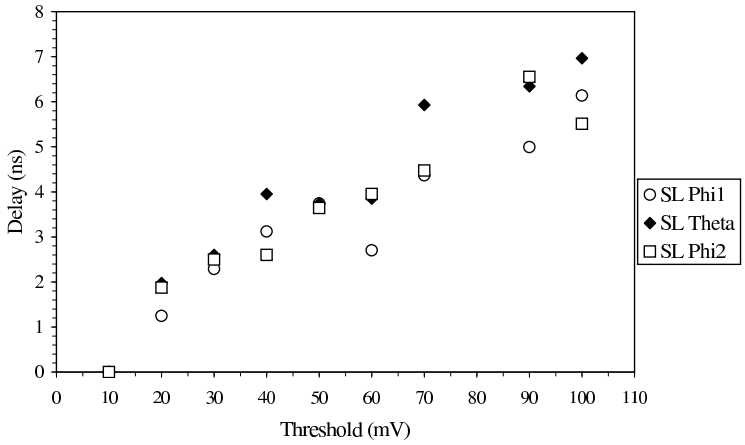

Figure 5: Dependence of the average delay time on the front-end discriminator threshold setting measured using cosmic-ray signals. The delay for a 10 mV threshold has been put arbitrary to zero.

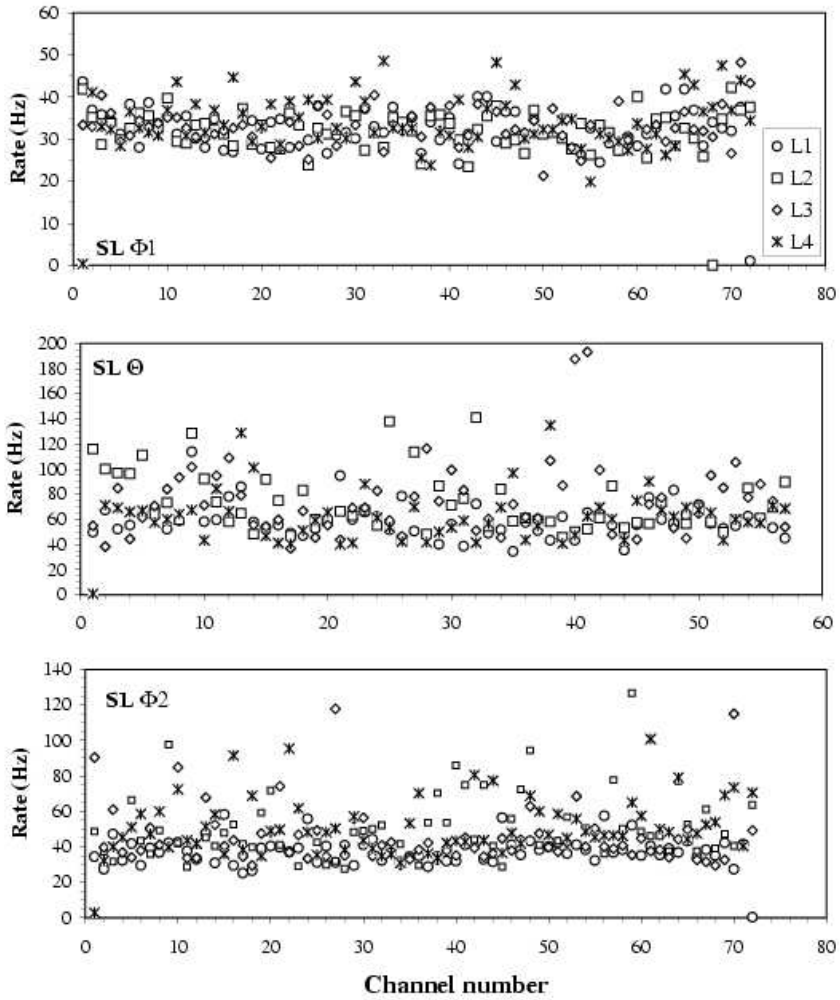

Figure 6: Noise rate at $V_{thr} = 15\ mV$ versus channel number for all layers of the three SLs of chamber MB3-011 at the standard HV setting.

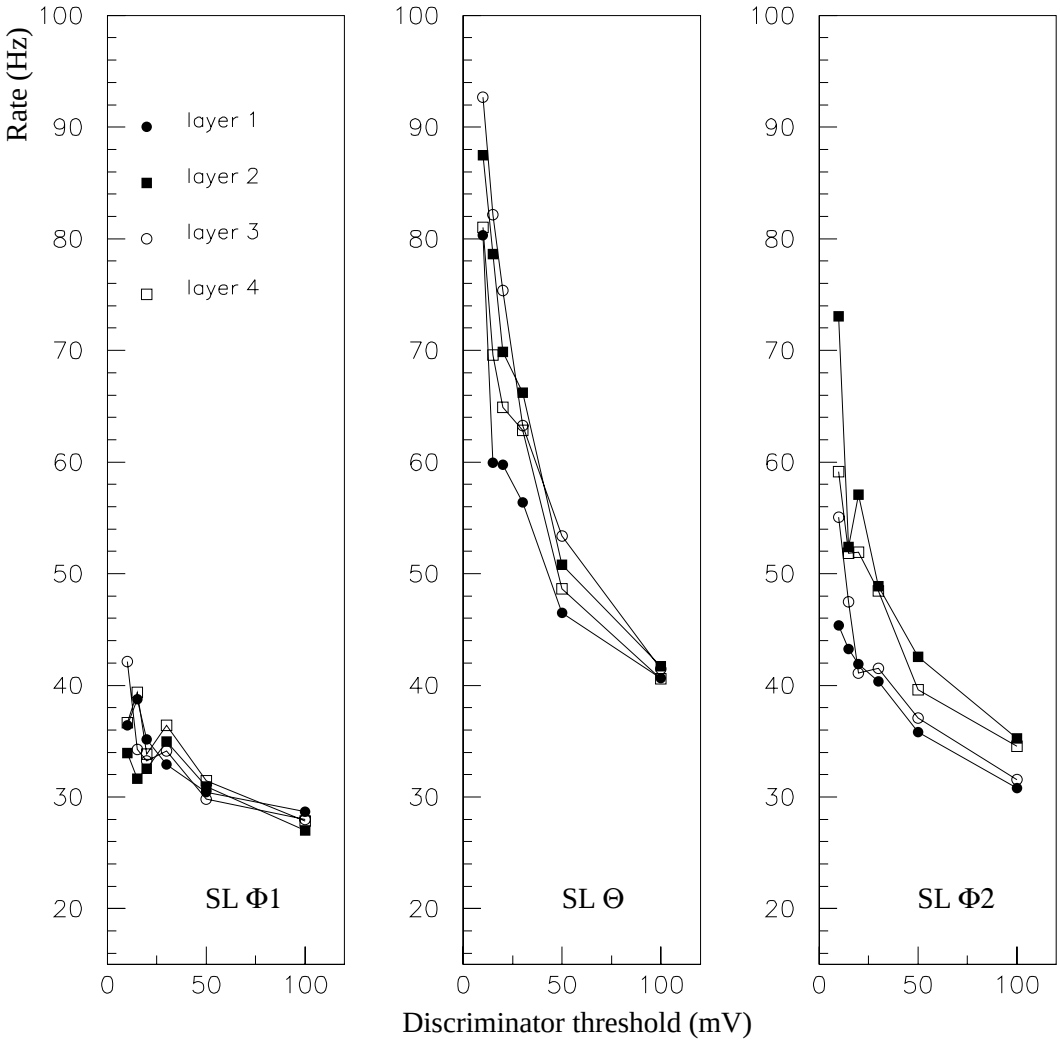

Figure 7: Dependence of the average noise rate of a single channel on the front-end discriminator threshold at the standard HV setting. Note that the noise rate also includes the cosmic-ray rate (on the order of 10 Hz/channel).

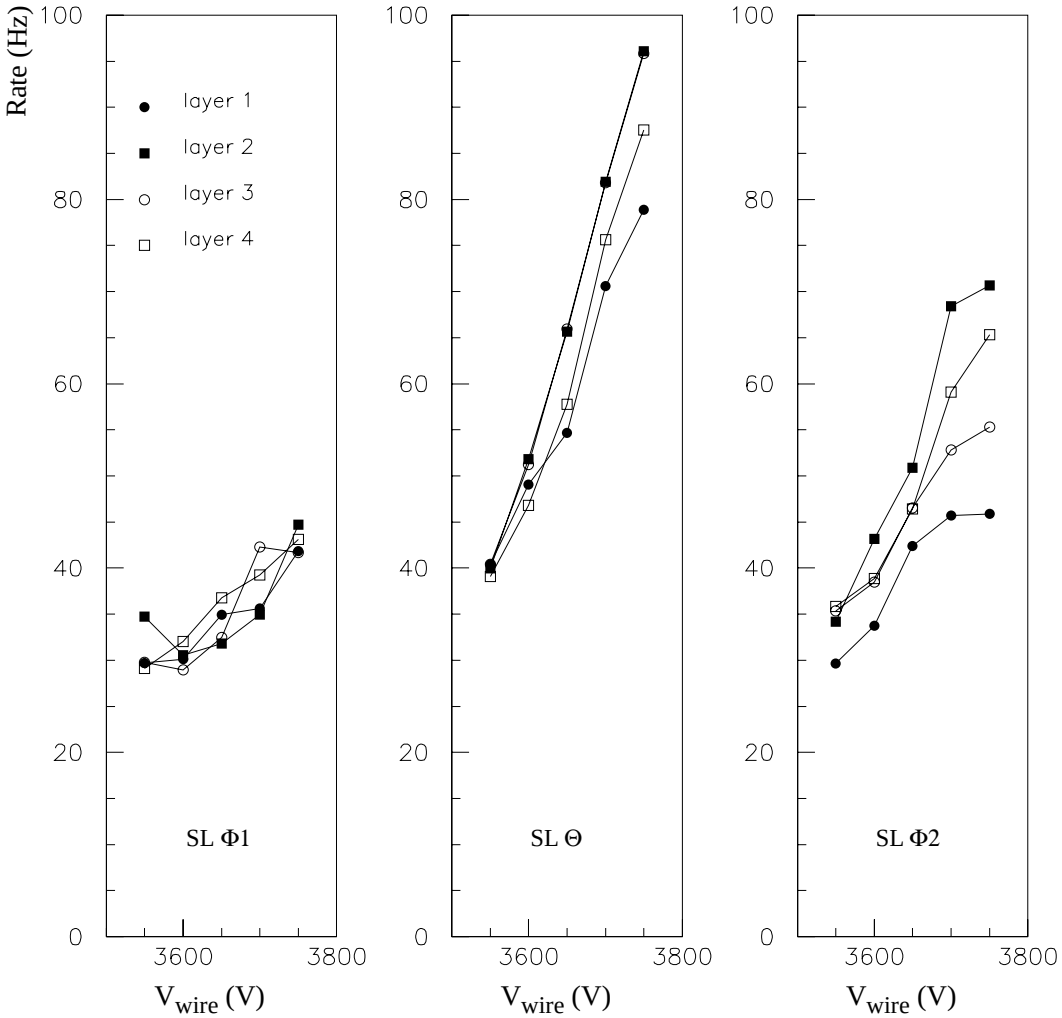

Figure 8: Dependence of the average noise rate on the wire voltage V_{wire} at 15 mV threshold ($V_{strip} = 1800\ V$, $V_{I-beam} = -1200\ V$) for the 3 SLs of chamber MB3-003.

The efficiency $\epsilon_\ell(x)$ in layer ℓ is determined as a function of the track extrapolated position x

$$\epsilon_\ell(x) = \frac{N_\ell}{N_\ell^{track}(x)} \tag{1}$$

where $N_\ell^{track}(x)$ is the number of tracks crossing layer ℓ at the position x and having a hit in each of the other three layers and N_ℓ is the subset of $N_\ell^{track}(x)$ composed of tracks with a fourth hit in layer ℓ within $\pm L$ from the track. In order not to depend on the details of the reconstruction, the fourth hit is not required to be included in the definition of the track.

We expect, as we have already measured in the past (see for example [8]), that the efficiency does not reach 100% because of the "shadow" caused by the I-beams, especially for tracks almost perpendicular to the layer. Figure 9 shows an example of the efficiency computed cell by cell in the four layers. Due to the applied algorithm, we expect to observe a lower efficiency for the first and last channels of the readout map, because a track can cross a neighbor cell which is not read out. For our acquisition scheme, this happens for channels at the border (channel 1) and at the half chamber (channels 36, 37).

Plots of the type shown in fig. 9 are computed for every produced chamber and stored in a database. They are used to quickly check the uniformity of the chamber and to cross check the presence of faulty channels. Faulty connections on either the HV or FE side have visible effects on these plots. The average efficiency is around 99%.

Sometimes it is also useful to check the efficiency within a single cell as a function of the track reconstructed position. Figure 10 shows this dependence for a fully-efficient chamber. The efficiency is always $> 98\%$ in the central region and starts to drop at a distance of about $2\ mm$ from the center of the cathode I-beam. This confirms that the inefficiency is totally due to the geometric acceptance given by the presence of the I-beams.

Hardware anomalies have visible effects on these plots. An example is given in fig. 11 which shows the first result obtained on chamber MB3-008. The first layer of superlayer $\Phi 2$ showed a reduced efficiency in the last 8 cells, as seen in the top plot. The middle plot shows, for comparison, the efficiency versus the drift position in a group of fully-efficient cells, while in the bottom plot one can see the behavior of not fully-efficient cells. It turned out that the bad cells had their cathodes disconnected from HV. The different electric field geometry caused the observed drop of efficiency in the vicinity of the I-beams. Nevertheless, it is worth noting that the cell efficiency remains as high as 80%.

Since the drop in efficiency corresponds exactly to the position of the I-beams, any shift of a layer of wires with respect to the others can also be observed as an asymmetry in the corresponding plot of fig. 10.

In fig. 12 the efficiency (1), averaged over a single layer, is plotted as a function of the track inclination with respect to the normal to the wire layer, for tracks passing close or far away from the I-beams. In the first case, the efficiency is 99.9% and independent of the inclination angle.

For tracks passing close to an I-beam, the efficiency decreases because a hit can be missed, depending on the track orientation and position. For angles $> 20^\circ$ the efficiency (1) is still greater than 98% since, for geometrical reasons, tracks produce hits in two contiguous cells of the same layer. For tracks with inclination $< 20^\circ$, the efficiency decreases as tracks approach the I-beam. At angles $< 3^\circ$ and in vicinity of an I-beam, the definition (1) of efficiency is inappropriate and yields poor results since the inefficiency due to the I-beam in layer i is correlated with the inefficiency of layer $i + 2$. We remind the reader that a track requires at least 3 hits and, therefore, no tracks are reconstructed near the I-beam, except perhaps when a δ-ray is produced.

A check of the dependence of the efficiency on the wire voltage was performed on a few chambers in order to validate the working point. The efficiency is known to depend, through the gas gain, on the "amplification voltage" $V_{ampl} = V_{wire} - V_{strip}$. A scan in V_{wire} was made, keeping V_{strip} fixed at $1800\ V$. The result is plotted, layer by layer for all three SL's, for chamber MB3-011 in fig. 14.

Figure 15 shows the efficiency at a standard HV setting as a function of the FE threshold. The efficiency changes in a negligible way when increasing the threshold up to $100\ mV$. The (small) efficiency loss at $10\ mV$ is probably due to the higher noise rate, which can generate fake tracks. In this threshold scan, the total number of hits decreases by about 9%, and is entirely due to the decrease of the number of after-pulses (defined as hits in the time window between T_{max} and $2\ T_{max}$, where T_{max} is the maximum drift time). The track reconstruction efficiency (number of reconstructed tracks/number of scintillator triggers) is about 70% (mainly because of the geometry of the scintillator system), independent of the threshold from 15 to $100\ mV$.

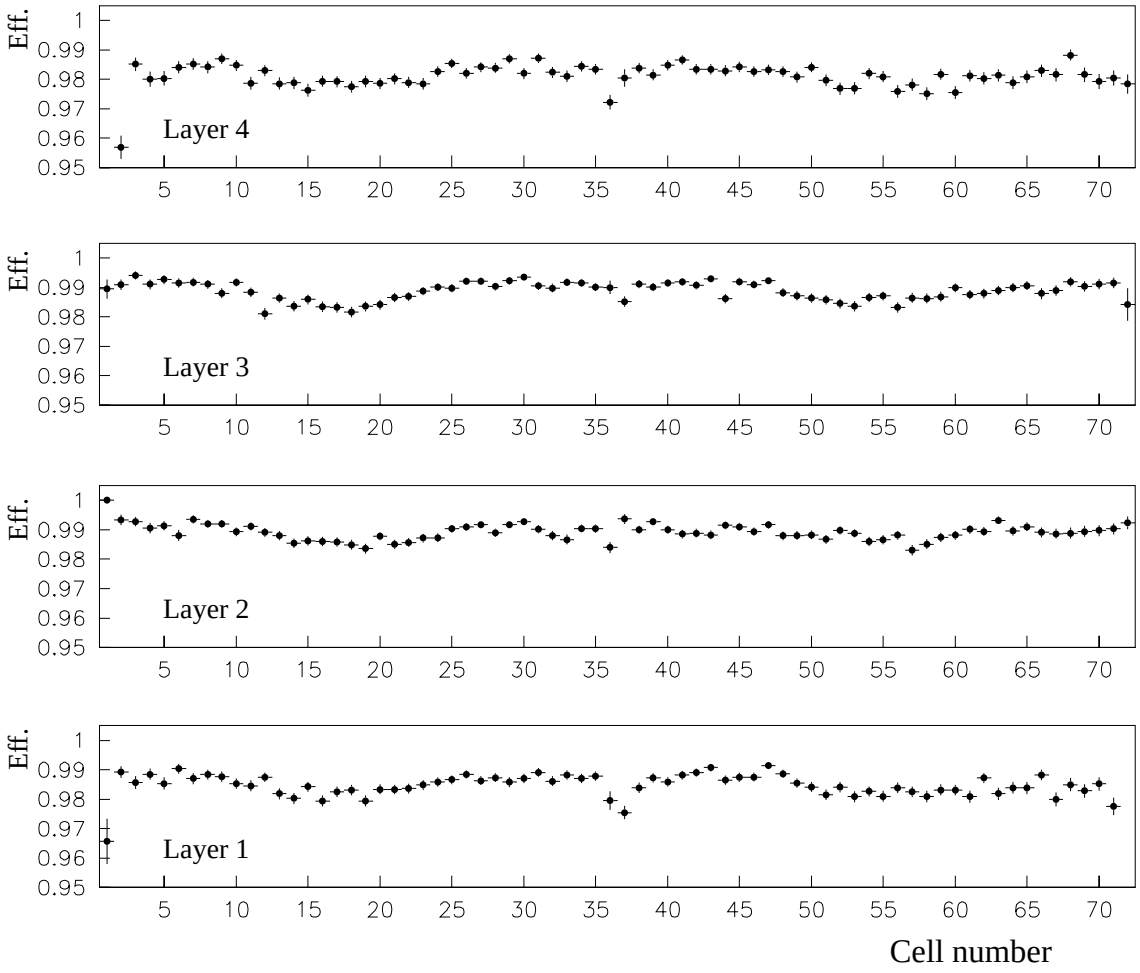

Figure 9: Efficiency versus cell number in the four layers of SL Φ1.

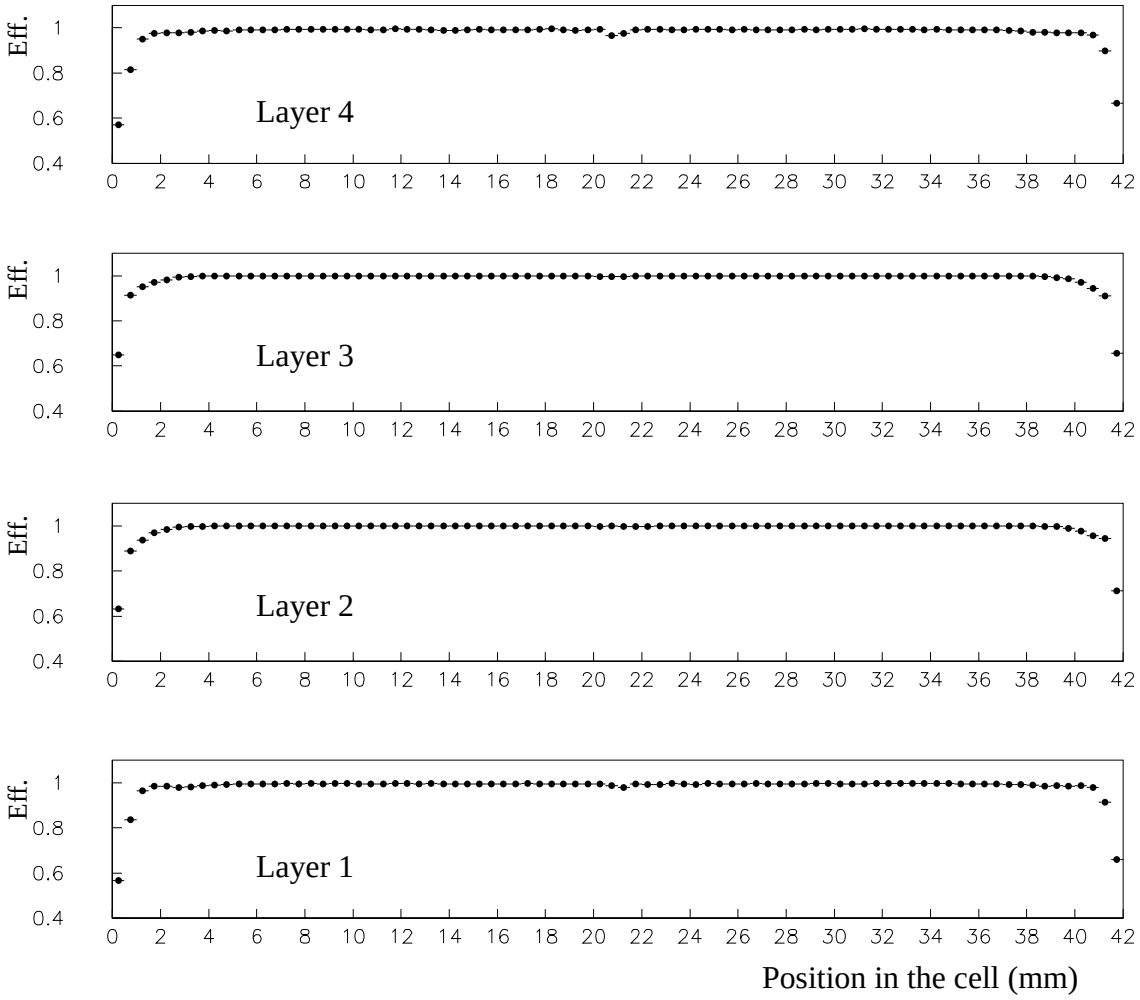

Figure 10: Average efficiency as a function of the reconstructed track position in the cells for the four layers of SL $\Phi 1$. The I-beams are at 0 and $42\ mm$, the wire at $21\ mm$.

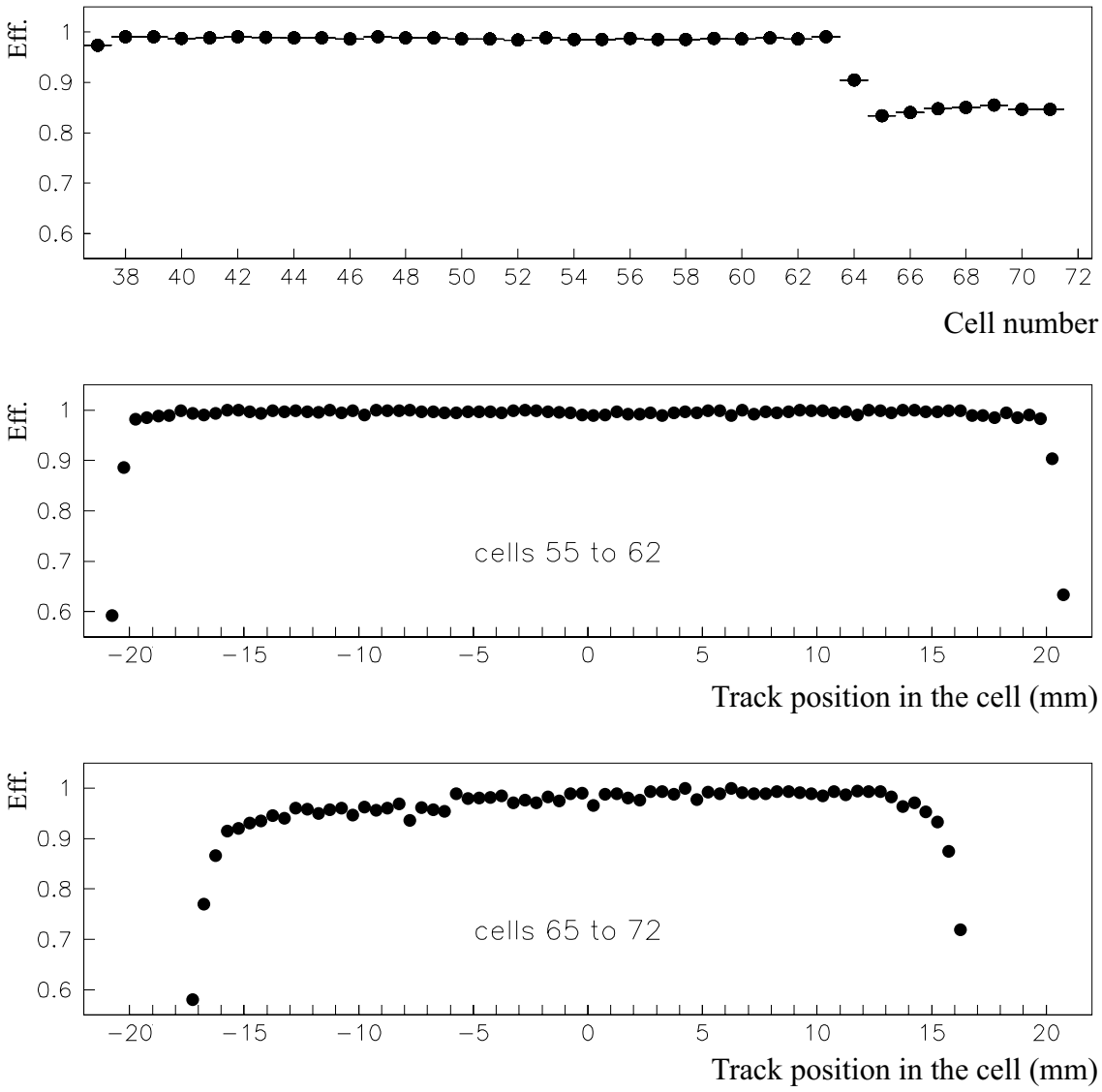

Figure 11: Top: efficiency versus cell number (early results on MB3-008); middle: efficiency vs. reconstructed track position, fully-efficient cells; bottom: efficiency vs. reconstructed position, not fully-efficient cells. The I-beams are at $\pm$ 21 mm, the wire at 0 mm.

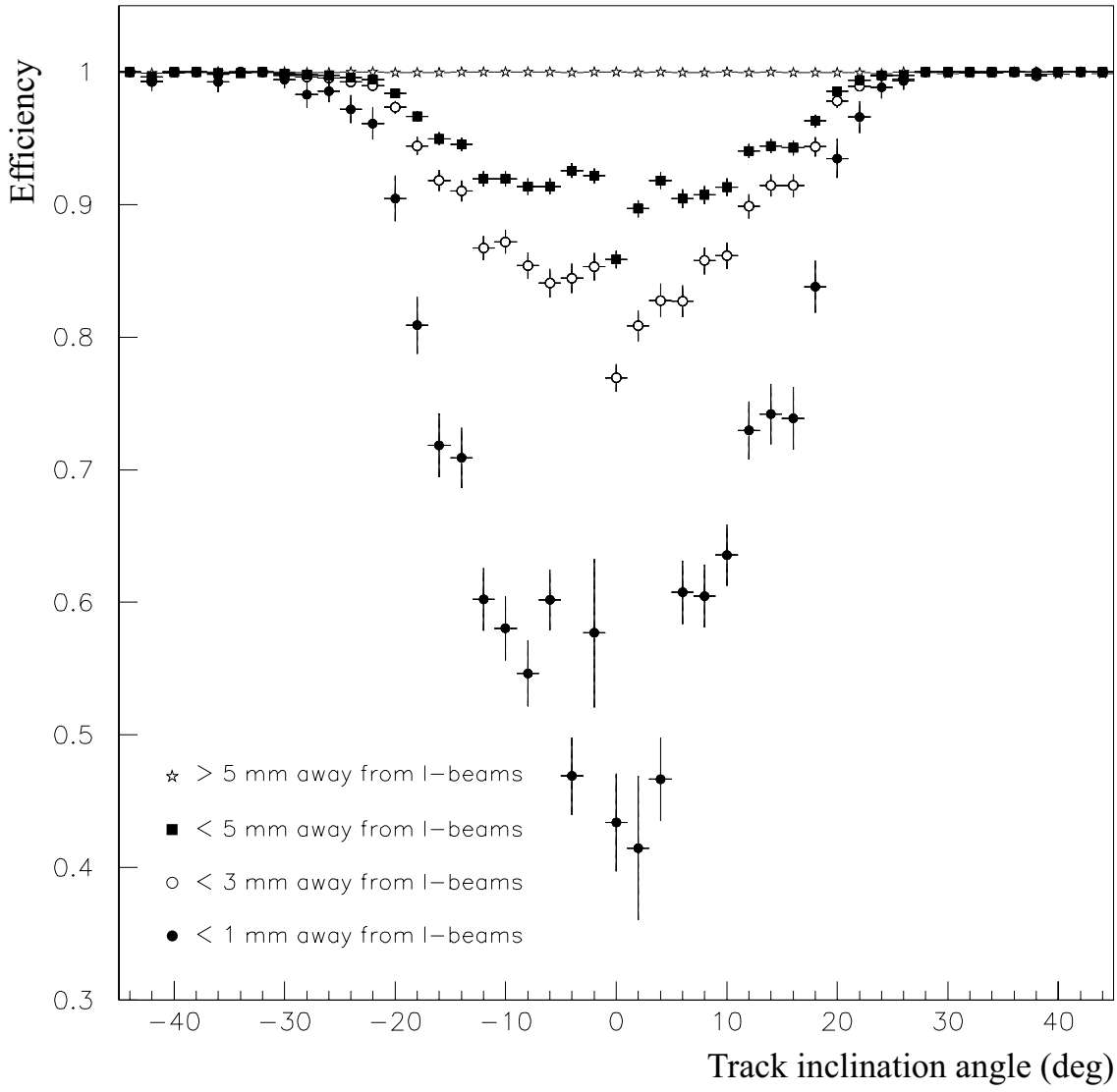

Figure 12: Average layer efficiency as a function of the fitted track inclination angle for tracks passing within four different ranges of distance from the I-beam. The distance is computed from the center of the I-beam.

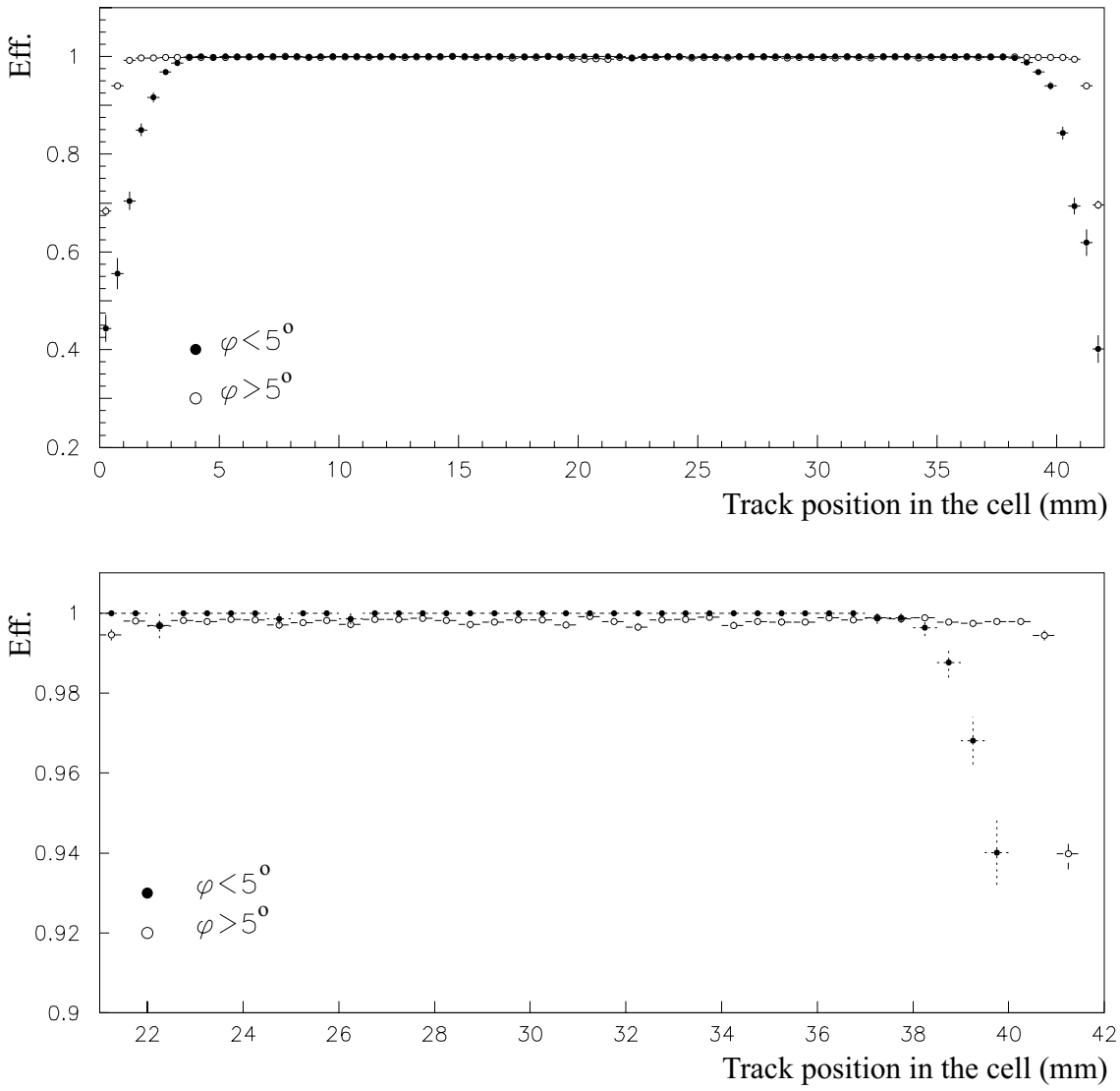

Figure 13: Efficiency versus reconstructed position for straight (•, angle $\leq 5°$) and inclined tracks (○, angle $> 5°$). The bottom figure is an expanded view of the top one near the I-beam position. The I-beams are at 0 and $42\ mm$, the wire at $21\ mm$.

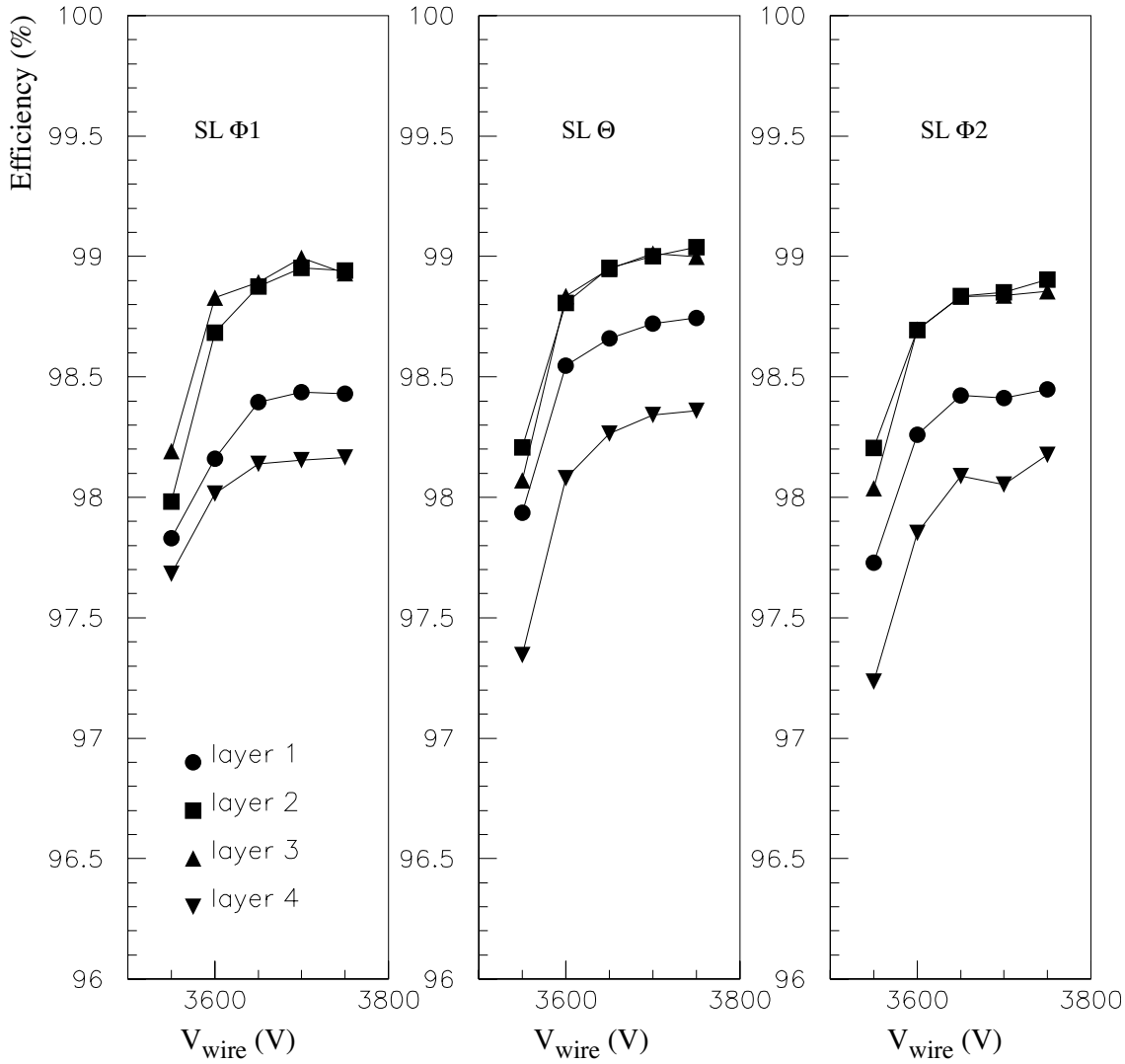

Figure 14: Average efficiency, layer by layer, as a function of the wire voltage V_{wire} at fixed $V_{strip} = 1800\,V$ and $V_{I-beam} = -1200\,V$, for the 3 superlayers of chamber MB3-011.

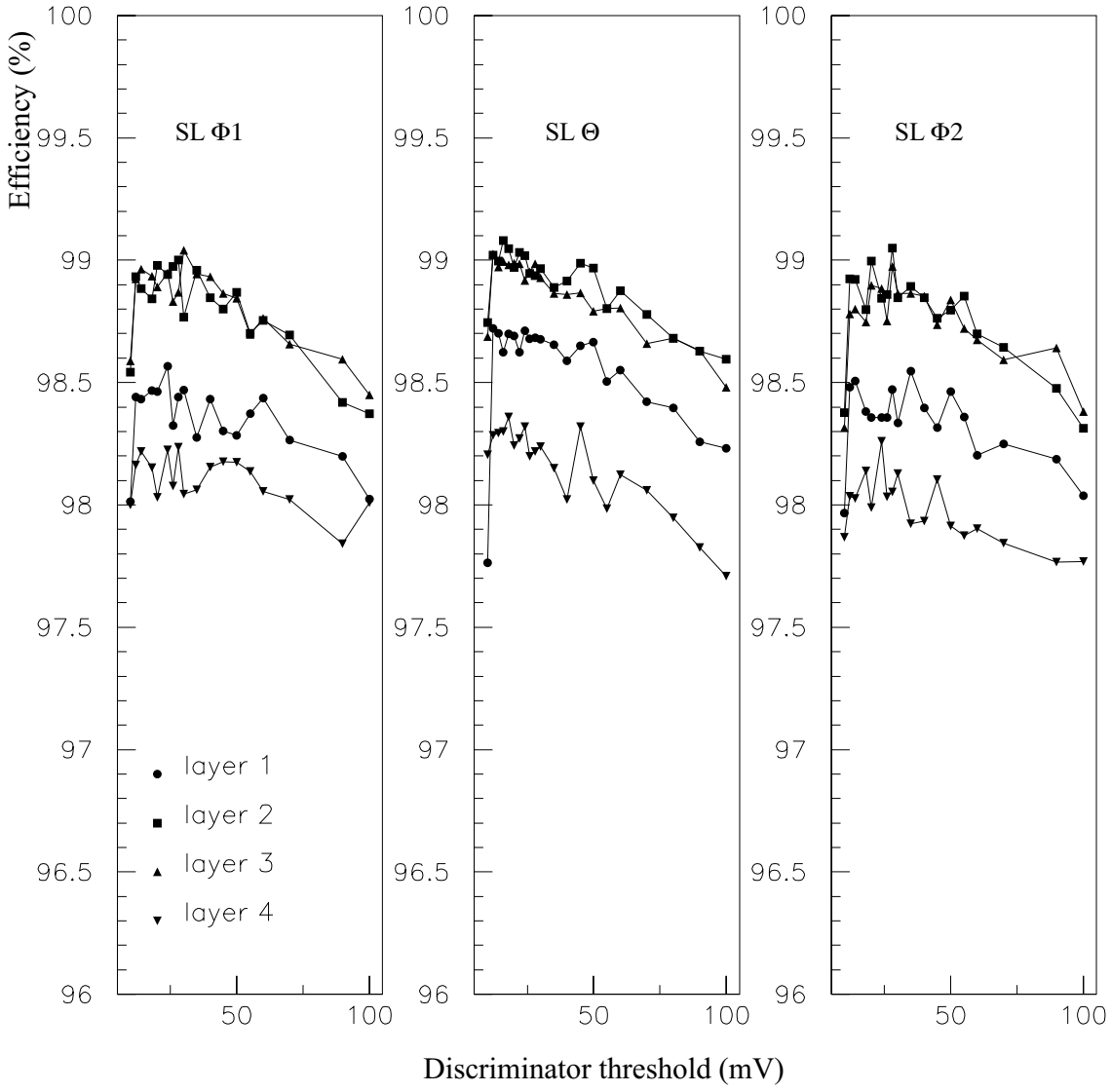

Figure 15: Efficiency versus discriminator threshold at the standard HV setting for all layers of chamber MB3-011.

For the first 11 chambers, 15 channels have been disconnected (mainly because of HV problems), corresponding to an average dead channel occurrence below 0.2%.

5 Test with cosmic rays: Mean Time and resolution studies

5.1 Definition

Resolution studies, a check of behavior uniformity of the SL, and a first glance at the geometric alignment of the layers inside a SL are performed using a Mean Time method. Assuming a uniform electron drift velocity, the Mean Time is the drift time corresponding to the half-wire pitch ($21\ mm$) and it is therefore inversely proportional to the drift velocity. Given 3 semi-cells in the same column in three successive layers j, $j+1$, $j+2$, for each track the Mean Time $MT_{i,L(R),1(2)}$ is defined as:

$$MT_{i,L(R),j} = \frac{T_i(j) + T_i(j+2)}{2} + T_i(j+1) \tag{2}$$

where i is the number of the cell in layer 1 (taken as the reference), $T_i(j)$, $T_i(j+1)$, and $T_i(j+2)$ are the drift times in the three cells, and the index L (Left) or R (Right) is given according to the hit position with respect to the wire in cell i. Layer $j+1$ is staggered by a half cell with respect to layers j and $j+2$. Simple geometrical considerations show that for a uniform drift velocity MT does not depend on the track angle or position. For each semi-column (left or right), two possible MTs can be obtained. The first, indexed with $j = 1$, is obtained by considering layers 1, 2, and 3, the second, indexed with $j = 2$, by considering layers 2, 3, and 4.

The MT is calculated for all tracks with 4 hits when all hits are in the same semi-column (which therefore is identified by the indexes i and L or R). This requirement automatically selects tracks with an angle $\leq\ 30^\circ$ with respect to the vertical (see also below) and causes the population of tracks passing close to the wire (and to the I-beams) to be depleted with respect to the rest of the cell. No other cuts are applied.

The drift time T_i is defined as $T_i = t_i - T_0$, where t_i is the hit time recorded by the TDC and corrected for the individual delay time $t_{0,i}$ (see sect. 3), and T_0 is the common delay time. While an accurate determination of T_0 is not needed for MT resolution studies and checks of uniformity behavior, it is indeed crucial for the calculation of the drift velocity and related quantities. However, it is also worth using the correct T_0 values to compare different chambers and different run conditions. T_0 is measured from a Gaussian fit of the derivative of the global drift time distribution (fig. 16): $T_0 = A - 3\sigma$, where A is the peak position and σ the peak standard deviation. The reason for this procedure is the difficulty in finding the start time of the drift time distribution. For a constant drift velocity one should expect a rectangular distribution. Since the electron avalanche develops at a distance on the order of several wire diameters ($50\ \mu m$ in our case), the region around the wire is inefficient when primary ionization electrons are generated there. This causes the depletion of events near the zero time. However, the next primary electron arriving at the wire is detected and this generates the accumulation of events at a drift time of about 10 ns. This time is proportional to the average distance between primary electrons, which is about 0.3 mm for our gas mixture [15].

Here we report the analysis results regarding the chamber FE sides, i.e. using scintillator group 5 for the Φ SLs and group 4 for the Θ SLs. The results regarding the HV side are compatible with the FE side, taking into account the poorer time resolution of the corresponding scintillators.

5.2 Correction for signal propagation time

Correct use of the MT requires a correction for the propagation time of the signal along the cell. In fact, the cell is a delay-line for the signal, and events occurring at different distances from the front-end amplifier, although at the same distance from the cell wire, reach the amplifier at different times. This time spread adds to the intrinsic time resolution if we do not take it into account. To measure the signal propagation time, we plot the mean value of the MT (i.e. averaged over all cells, over all angles and over all positions inside the cell) versus the position along the wire. If we are looking at a SL Φ, the position along the wire is obtained from the SL Θ, and vice-versa. The result is shown in fig. 17. The slope of the linear fit is the signal propagation velocity v_{signal}, which gives $v_{signal} = 0.244\ m/ns$, consistent with the previous determination reported in [16, 10] and with test bench measurements [17]. The effect of the propagation time can be clearly seen in fig. 17, where the distribution of the average MT is plotted before and after the correction. The standard deviation of the distribution improves by more

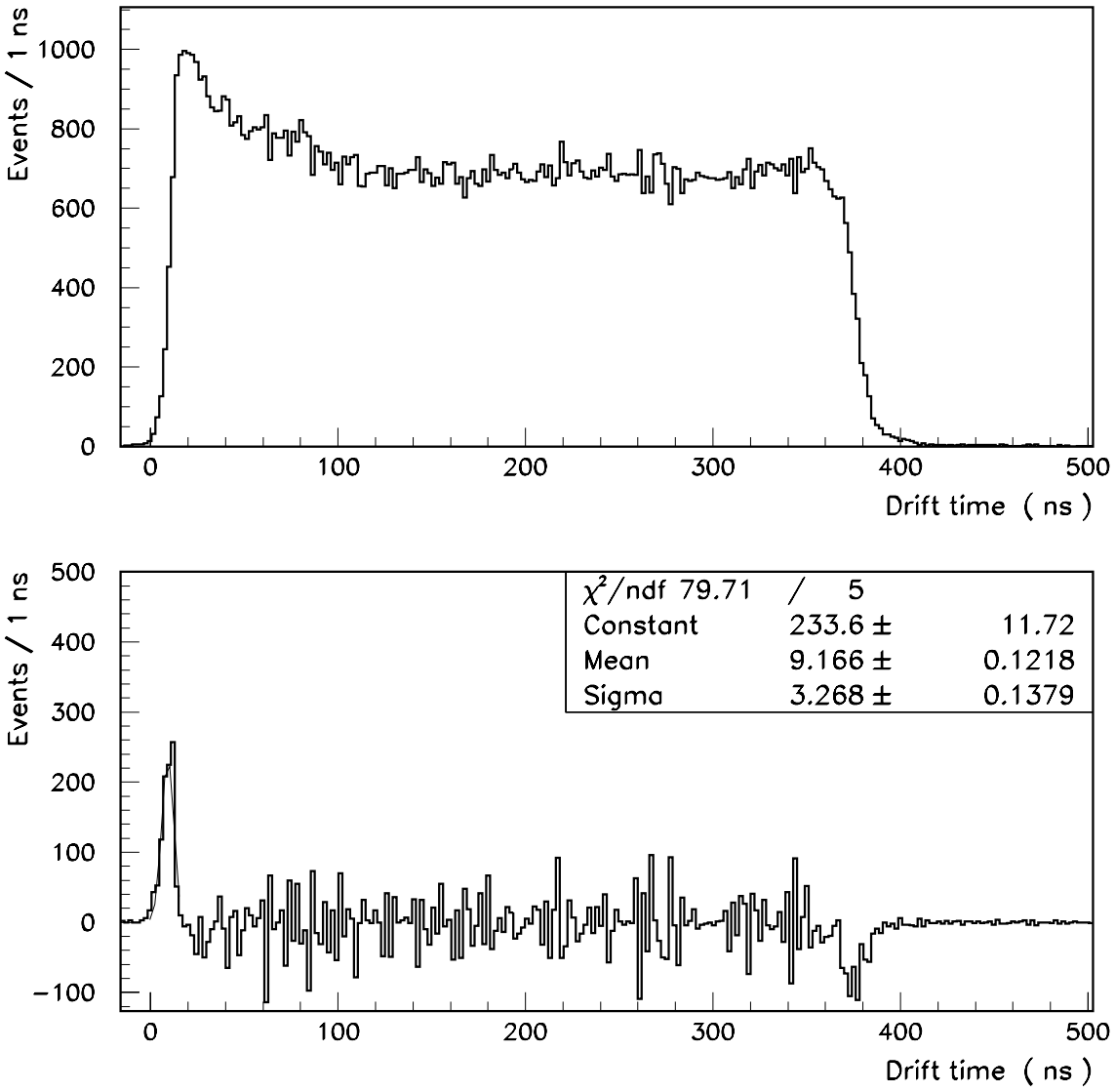

Figure 16: Distributions at the standard HV and threshold setting for: (top) drift time, and (bottom) its derivative, with a Gaussian fit of the peak after the T_0 subtraction.

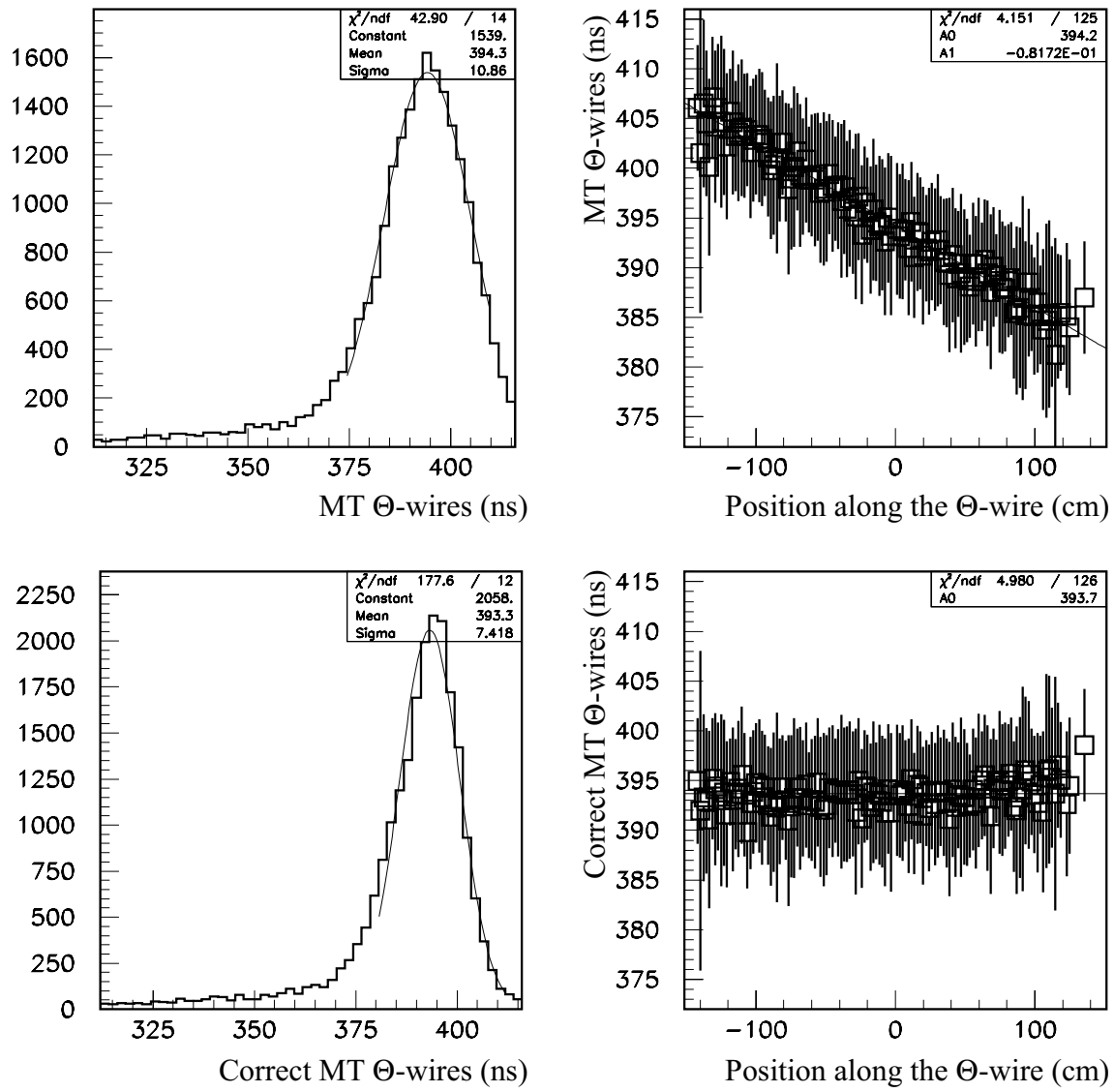

Figure 17: MT distributions (left) and the MT dependence on the position along the wire (right) before (top) and after (bottom) the correction for signal propagation time.

than 30%, decreasing from about $10\ ns$ to about $7\ ns$. Note that the local BTI trigger [5] cannot compensate for the signal propagation time, but will see it as a phase shift.

From here on, we always correct the drift time T_i for the signal propagation time.

5.3 MT vs. High Voltage, track inclination, and reconstructed position

For each cell i the mean time distributions are computed. Due to δ-ray production, the distribution is not symmetric with respect to the peak but has a non-Gaussian tail on the left side of the peak. The right side of the distribution behaves well and can be fitted to a Gaussian function (see for example fig. 17). The mean value of the Gaussian is taken as the effective MT value, while the standard deviation is used for resolution studies.

The dependence of the mean time MT and the MT resolution σ_{MT} on the cell number i is plotted in fig. 18. We have to remember that σ_{MT} is biased by the scintillator time resolution, which is rather poor, especially for the Θ SL. Therefore, we look at the MT resolution only to check the uniformity in a chamber and the consistency from chamber to chamber.

Figure 19 shows the dependence of the average $MT_{1,L}$ and $MT_{2,L}$ and MT resolution on the wire voltage V_{wire} for chamber MB3-011. Note that for the Θ SL, the MT resolution is almost independent of V_{wire}, being completely dominated by the trigger resolution. We checked that tracks triggered by a small plastic scintillator with a good time resolution ($\approx\ 1\ ns$) have a MT resolution around $4\ ns$ (at the standard HV setting), as expected from previous test beam runs [7, 8, 9, 10]. The observed dependence of the MT on V_{wire} agrees well with our previous measurements reported in [8]. Such behavior can be attribuited to the variation of the average electron drift velocity in the gas. Other contributions are possible, as for example the fact that V_{wire} determines the wire gain, which influences the signal shape (risetime). This time variation, known as time walk, has been measured to be $2\ ns$ for a $15\ mV$ threshold in the gain range we span by changing V_{wire} [11], and reflects into a $4\ ns$ change of the MT.

Figure 20 shows the variation of MT_1 with the track inclination angle in the plane perpendicular to the wires and with respect to the vertical direction. The angle is obtained by fitting the hits in the same SL to a straight line. It's worth noting that the apparent MT and, therefore, the drift velocity, is nearly flat up to 15° and changes by less than 3% for angles up to 30°. On the contrary, the MT does not depend on the track angle with respect to the vertical plane containing the wire (fig. 21).

From the fit of the track we also obtain the closest distance of the track from the wire. The plot of the MT (averaged over all angles) can disclose anomalous behavior inside the cells, analogously with what shown in sect. 4. In fig. 22 the behavior of the average MT and the MT resolution are reported as a function of the reconstructed drift distance for almost perpendicular tracks (inclination $\leq 4^\circ$). Near the wire and the I-beams the MT value and resolution are not calculated because of the poor statistics available with the applied cuts.

5.4 Layer misalignment

Systematic differences for all semicolumns in a SL between MT_L and MT_R and between MT_1 and MT_2 are caused by misalignments of the layers (see also [18]). Recalling eq. (2) and the relationship between MT and electron drift velocity v_{drift}, the variations ΔMT of the mean time due to a global misalignment Δl_j of layer j are:

$$v_{drift}\ \Delta MT_{L,1} = -v_{drift}\ \Delta MT_{R,1} = \frac{\Delta l_1 + \Delta l_3}{2} - \Delta l_2$$

$$v_{drift}\ \Delta MT_{L,2} = -v_{drift}\ \Delta MT_{R,2} = -\frac{\Delta l_2 + \Delta l_4}{2} + \Delta l_3$$

where the MTs are averaged over all cells. Therefore, the quantities

$$\Delta MT_j = MT_{L,j} - MT_{R,j} \quad (j = 1, 2)$$

$$\Delta MT_{L(R)} = MT_{L(R),1} - MT_{L(R),2}$$

are proportional to the layer misalignments, namely

$$v_{drift}\Delta MT_1 = \Delta l_1 + \Delta l_3 - 2\ \Delta l_2$$

$$v_{drift}\Delta MT_2 = -(\Delta l_2 + \Delta l_4) + 2\ \Delta l_3$$

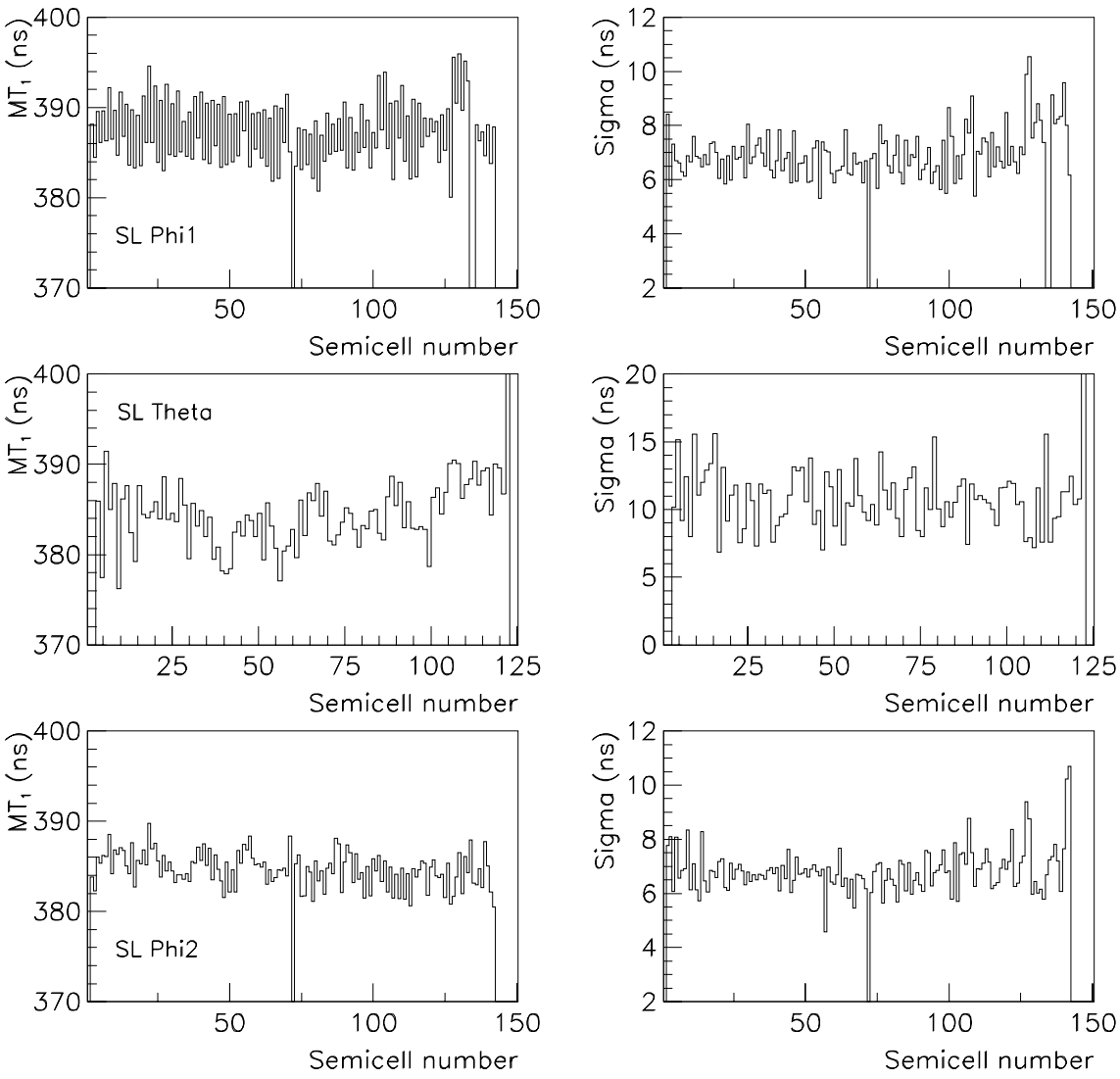

Figure 18: Dependence of MT_1 (both $MT_{1,L}$ and $MT_{1,R}$) and the MT_1 resolution for all SLs of chamber MB3-011 (at the standard HV and threshold setting) on the semicell number.

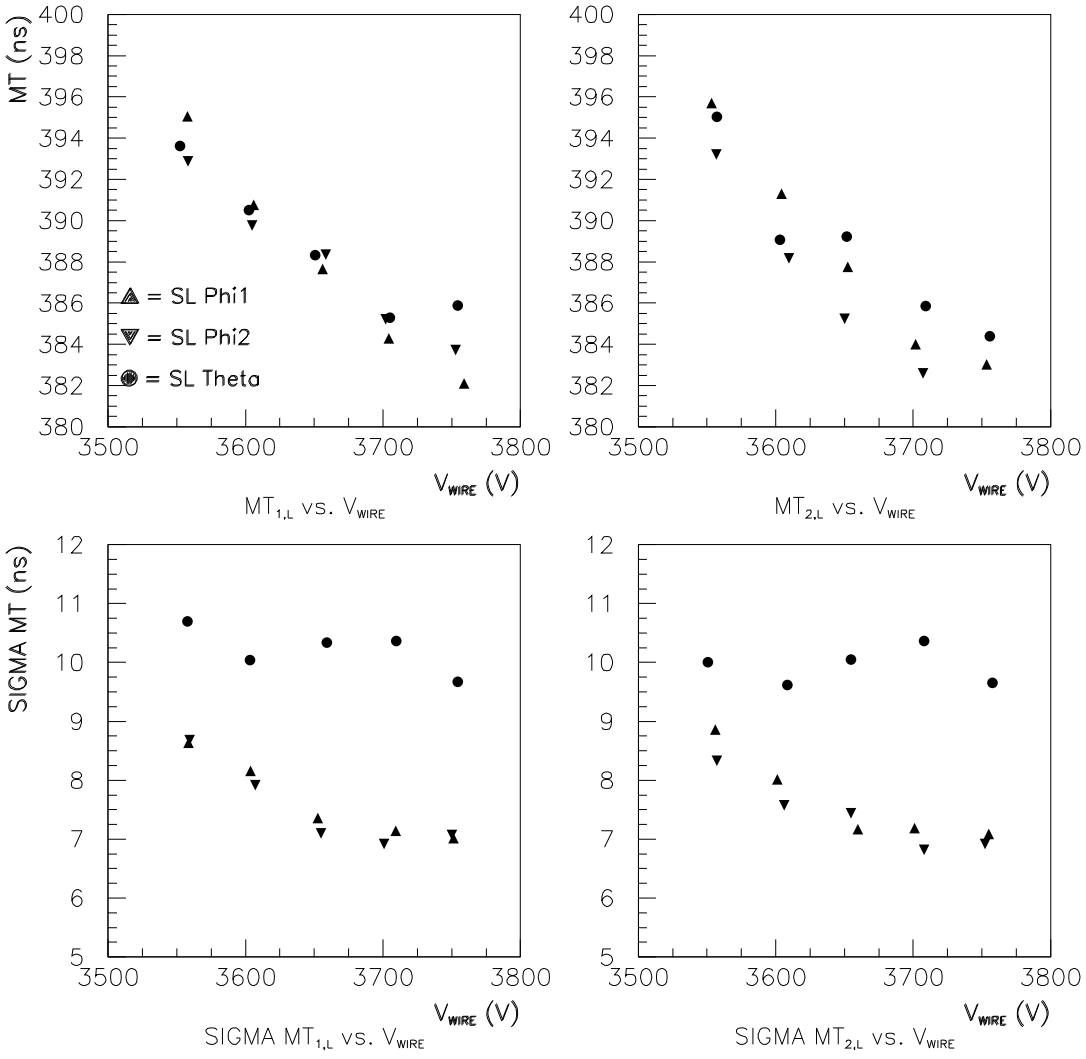

Figure 19: Dependence of $MT_{1,L}$, $MT_{2,L}$ and the MT resolution (trigger resolution not subtracted) on the wire voltage V_{wire} for the 3 SLs of chamber MB3-011.

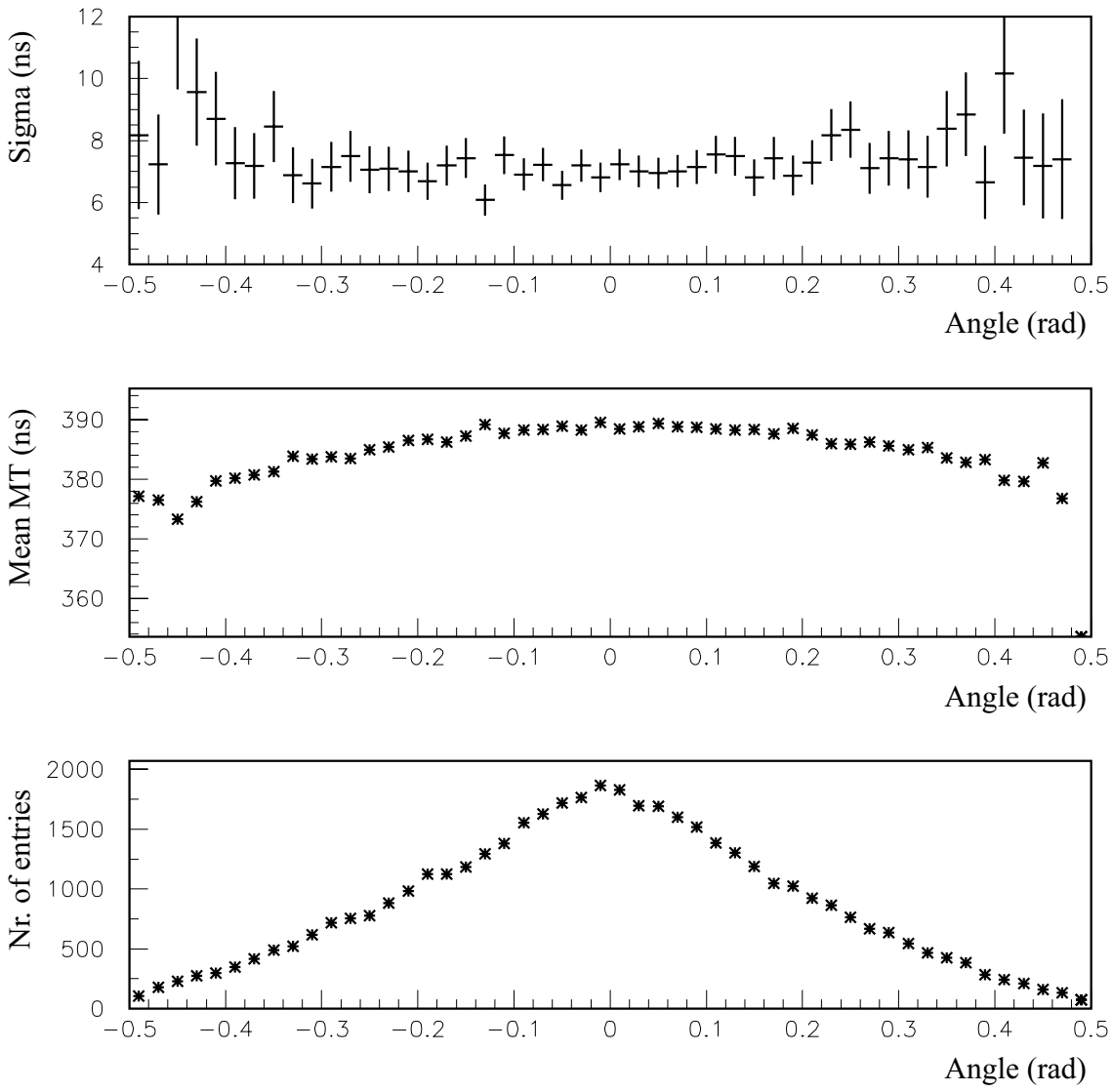

Figure 20: Dependence of the MT on the inclination angle of the cosmic-ray tracks in the plane perpendicular to the wires. Top plot: MT resolution (trigger resolution not subtracted); middle plot: average MT; bottom plot: number of entries. The range spans tracks up to $\pm$ 29° in inclination angle.

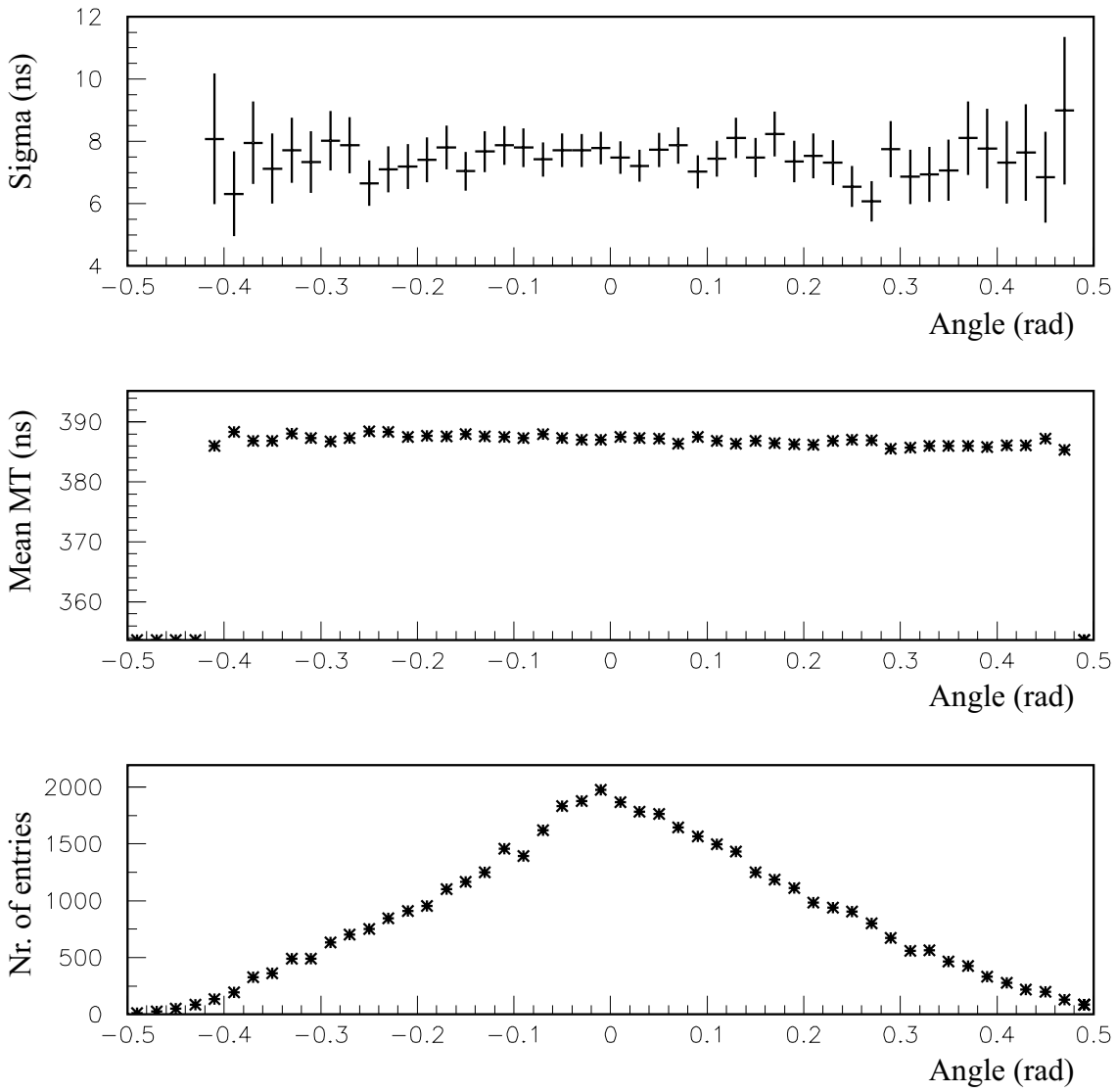

Figure 21: Dependence of the MT on the inclination angle of the cosmic-ray tracks with respect to the plane containing the wires. Top plot: MT resolution (trigger resolution not subtracted); middle plot: average MT; bottom plot: number of entries. The range spans tracks up to $\pm\ 29^{\circ}$ in inclination angle.

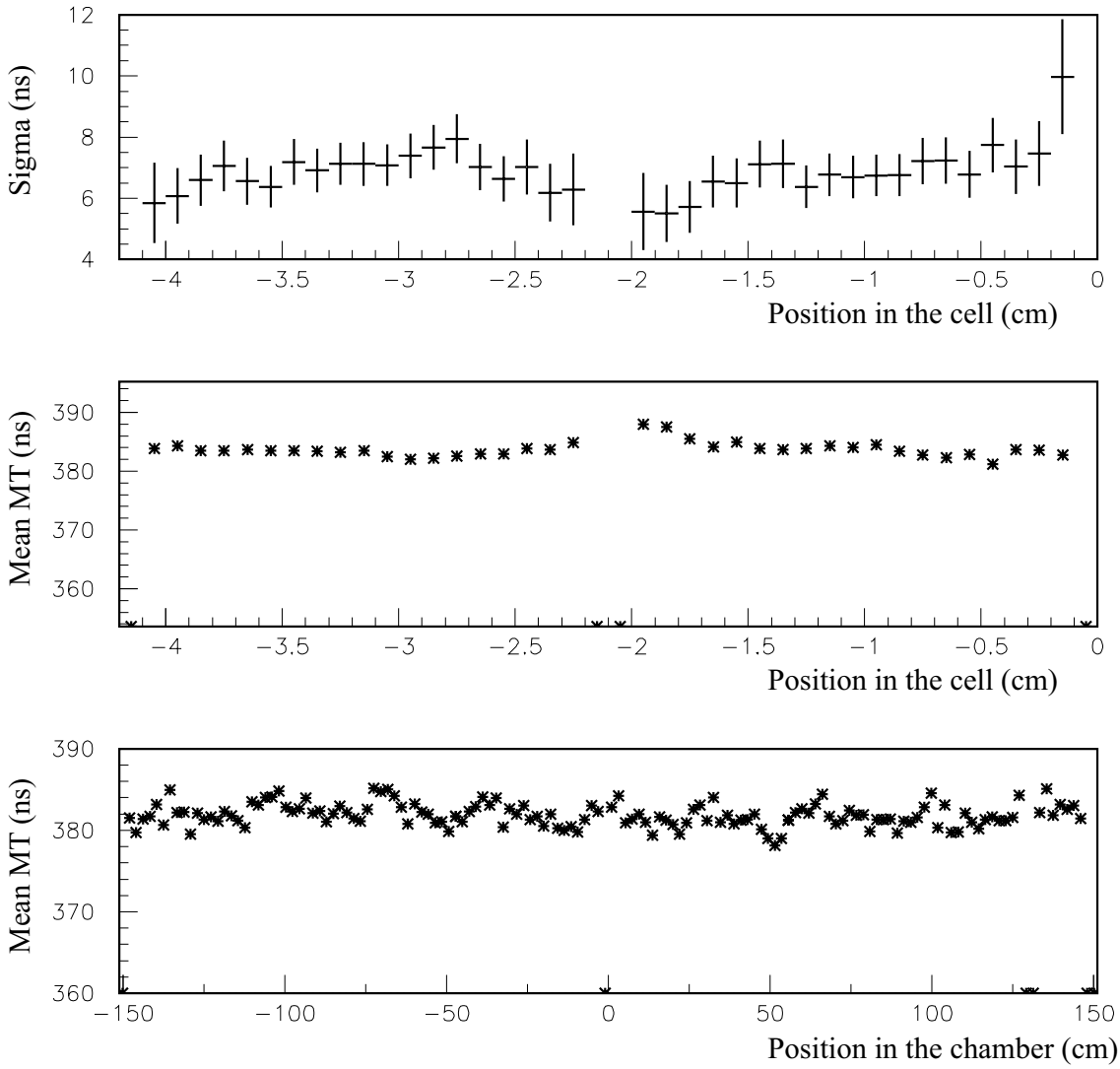

Figure 22: Dependence of the MT resolution (top) and the average MT value (center) on the position of the track in the cell (the I-beams are at 0 and $-4.2\ cm$, the wire is at $-2.1\ cm$). The bottom plot shows the dependence of the MT value on the absolute track position in the chamber.

$$v_{drift}\Delta MT_L = -v_{drift}\Delta MT_R = \frac{1}{2}(\Delta l_1 - \Delta l_2 - \Delta l_3 + \Delta l_4).$$

Actually, the third equation is not independent of the other two, therefore the system does not have a unique solution. Nonetheless, values of ΔMT_1, ΔMT_2 or $\Delta MT_{L(R)}$ different from zero (within the errors) are evidence that at least one layer is not aligned, and give the order of magnitude of the shift of the layers inside the SL (see table 2). The absolute shifts of the layers can be obtained by means of a recursive procedure which will be described in a forthcoming paper.

Table 2 summarizes the MT measurements for the first MB3 chambers produced at Legnaro. The maximum observed misalignment is about $6\ ns$, equivalent to a layer shift on the order of a few hundred microns.

5.5 MT vs. gas pressure

The drift velocity and wire gain depend on the gas pressure inside the chamber for fixed electrode voltages. Therefore, we expect that the MT values will also change accordingly. We took data at different values of gas pressure in the chamber, from $1005\ mbar$ to $1075\ mbar$. The variation $\Delta MT$of the MT (with respect to the value at $1020\ mbar$, which is our standard pressure condition) with the gas pressure is shown in fig. 23. The effect is small but measurable. The drift velocity varies by less than 1% for $\Delta P \approx 70\ mbar$.

It is interesting to compare this graph with fig. 19, which shows the variation of the MT with the wire voltage V_{wire}. Since the drift velocity (along with other physical quantities such as diffusion and wire gain) is a function of the ratio E/P, where E is the electric field and P the gas pressure, we expect that the relative variation $\Delta MT/MT$ will be proportional to the relative variation $\frac{\Delta(E/P)}{E/P}$. Apparently this is not the case. At the standard HV setting, the average electric field is around $2.3\ kV/cm$ and is proportional to $V_{wire} - V_{cathode}$. The change of V_{wire} in fig. 19 corresponds to a relative variation $\Delta E/E = \Delta V_{wire}/V_{wire} = 5.4\%$ (taking as reference the point at the standard HV setting and at $P = 1020\ mbar$). In fig. 23 the relative pressure variation is $\Delta P/P = 7\%$. The MT variations ΔMT are respectively $6\ ns$ (the contribution from the FE time walk has been subtracted) and $3\ ns$ and miss by about a factor of 2 the proportionality with $\frac{\Delta(E/P)}{E/P}$. The data are summarized in table 1. A possible explanation is that a variation of V_{wire} produces not only a change in E/P but also a change in the electric field lines and therefore in the path of the ionization electrons. On the other hand, a variation in the pressure changes the ratio E/P without modifying the electron path.

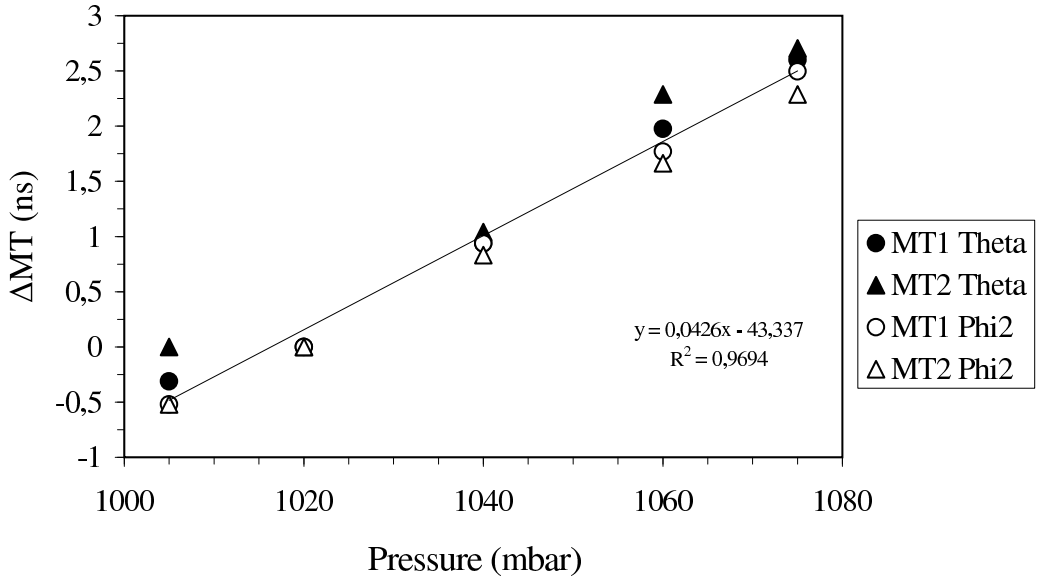

Figure 23: Variation of the MT as a function of the gas pressure with respect to the MT value at $P = 1020\ mbar$. The data refer to chamber MB3-006 at the standard HV and threshold conditions.

Table 1: Variation of the MT with the ratio E/P.

$\Delta E/E(\%)$	$\Delta P/P(\%)$	ΔMT (ns)	$\frac{\Delta(E/P)}{E/P}(\%)$	$\Delta MT/MT(\%)$
5.4	0	–6	5.4	–1.6
0	6.9	3	–6.9	0.8

Table 2: Summary of MT results for the first 11 MB3 chambers. All data are in ns. Trigger resolution is not subtracted. Chambers MB3-002 and MB3-003 were run with a variable gas pressure. The gas composition of the last two chambers was slightly different from the CMS standard mixture.

Chamber, SL	MT_1	σ_1	$MT_{1,L}$	$MT_{1,R}$	MT_2	σ_2	$MT_{2,L}$	$MT_{2,R}$	ΔMT_1	ΔMT_2
MB3-002, Φ1	385.1	8.63	383.4	386.8	385.6	8.53	385.7	385.5	–2.5	0.1
MB3-002, Θ	388.9	9.67	386.9	390.7	388.4	9.88	385.2	391.2	–3.5	–6.1
MB3-002, Φ2	383.6	8.42	383.0	384.2	383.9	8.11	382.9	384.7	–1.2	-1.8
MB3-003, Φ1	373.6	7.9	373.2	374.0	374.1	8.0	373.6	374.6	-0.8	1.1
MB3-003, Θ	375.2	9.6	373.0	377.1	378.0	9.6	374.7	380.8	–4.7	–4.1
MB3-003, Φ2	374.6	8.1	374.2	374.9	374.9	7.7	375.1	374.7	-0.7	0.3
MB3-004, Φ1	380.1	7.2	380.2	380.0	380.2	7.4	379.4	381.1	0.1	–1.7
MB3-004, Θ	394.0	9.5	394.1	393.8	394.1	9.3	395.6	392.4	0.0	2.9
MB3-004, Φ2	380.3	7.5	378.0	382.8	380.5	8.0	377.7	383.6	–4.8	–5.7
MB3-005, Φ1	379.1	7.0	379.8	378.4	379.2	6.7	379.9	378.6	1.6	1.4
MB3-005, Θ	376.8	10.2	376.2	377.4	377.4	10.0	378.1	376.8	–1.6	0.7
MB3-005, Φ2	377.7	7.5	375.1	380.3	377.6	7.1	375.8	379.5	–5.3	–3.7
MB3-006, Φ1	383.2	7.1	382.9	383.4	383.6	6.9	383.3	383.8	–0.6	–0.3
MB3-006, Θ	382.4	9.9	382.2	382.5	382.9	9.5	383.3	382.5	–0.8	0.5
MB3-006, Φ2	382.3	7.4	379.5	385.1	382.4	7.4	379.8	385.0	–5.5	–5.2
MB3-007, Φ1	381.1	7.2	380.5	381.6	381.4	7.1	379.7	382.9	–1.0	–3.1
MB3-007, Θ	381.5	10.2	381.0	381.9	382.0	10.1	381.9	382.0	–1.1	–1.0
MB3-007, Φ2	381.7	7.2	379.8	383.6	381.8	7.3	379.7	384.0	–3.8	–4.1
MB3-008, Φ1	381.5	7.0	380.7	382.2	381.7	6.9	381.1	382.3	–1.6	–1.4
MB3-008, Θ	381.3	10.0	381.7	381.0	382.5	9.5	382.6	382.4	–0.4	0.5
MB3-008, Φ2	381.0	7.0	381.1	380.8	380.8	6.8	380.6	381.2	0.2	0.6
MB3-009, Φ1	380.4	7.1	380.6	380.1	380.5	7.0	379.9	381.1	0.5	–1.0
MB3-009, Θ	378.9	10.0	377.9	379.7	379.8	10.0	379.6	380.1	–2.0	–0.7
MB3-009, Φ2	379.4	7.0	378.9	379.9	379.4	6.9	379.2	379.7	–0.9	–0.6
MB3-010, Φ1	386.0	6.9	385.5	386.6	386.0	7.2	387.2	384.9	–1.0	2.2
MB3-010, Θ	382.6	10.0	382.8	382.3	383.2	10.2	382.8	383.7	0.3	–0.9
MB3-010, Φ2	384.0	7.0	382.9	385.0	384.1	6.7	383.6	384.6	–2.1	–1.1
MB3-011, Φ1	387.5	7.8	384.9	390.2	387.3	7.1	386.0	388.4	–5.4	–2.5
MB3-011, Θ	384.5	10.5	384.3	384.6	385.0	9.5	384.9	385.1	–0.2	–0.2
MB3-011, Φ2	384.8	7.0	384.4	385.1	384.7	6.8	383.6	385.7	–0.7	–2.3

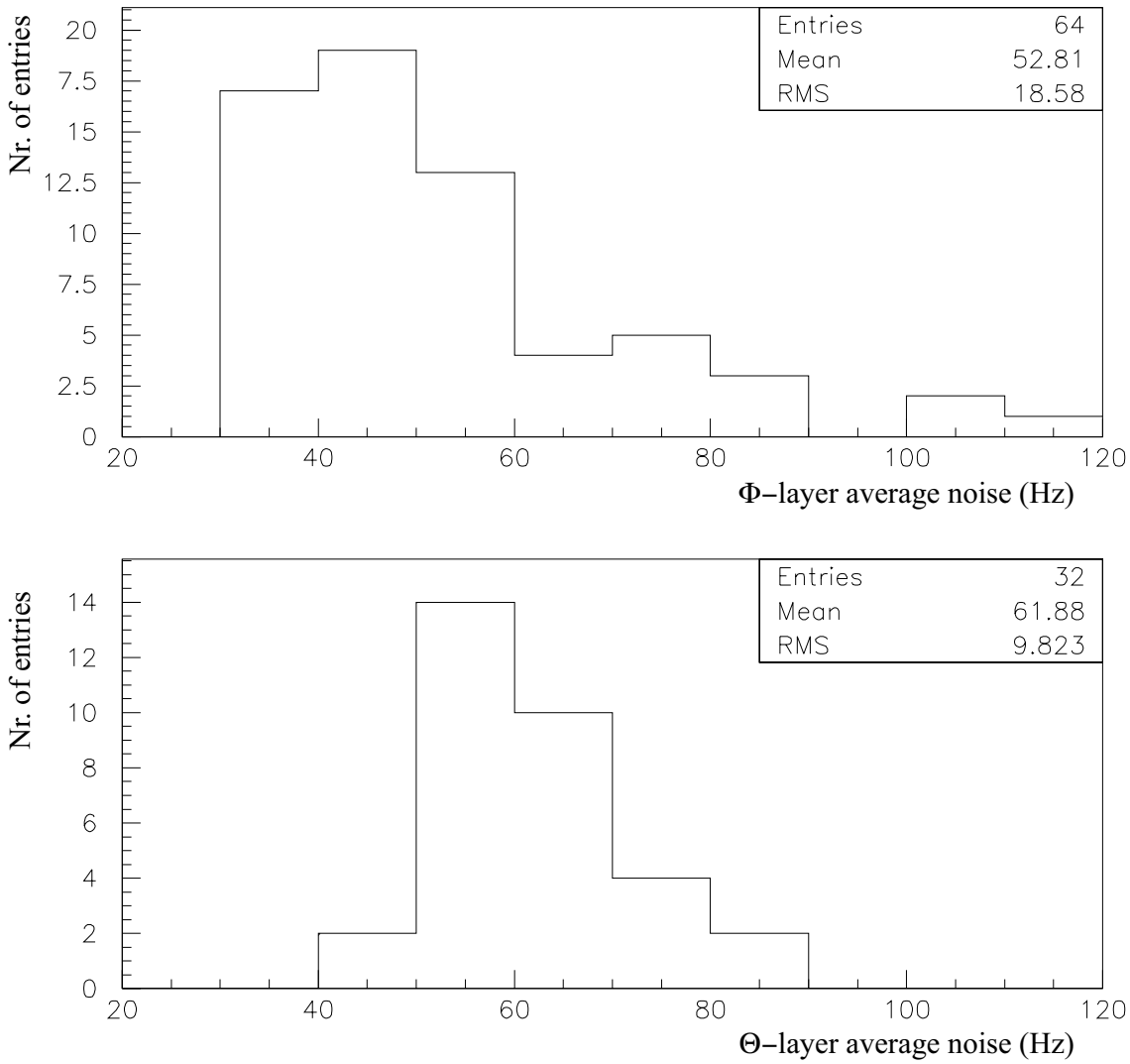

Figure 24: Distribution of the average Φ-wire (top) and Θ-wire (bottom) noise rate, averaged over each layer, for the first 11 MB3 chambers built at Legnaro.

6 Conclusions

In this note we have presented the results of an analysis performed on each chamber built at the Legnaro INFN Laboratories which were used to disclose possible defects in the construction or in the electrical cabling. We demonstrated that the procedure is very effective in finding disconnected electrodes, checking the global uniformity and performance of the chambers, and identifying misaligned layers. Moreover, we have extensively studied the main features of the detector over its entire size and at the same time using all possible track orientations. Such analysis was never done before on CMS MB chambers and is complementary to tests using collimated beams from accelerators.

We find that the measured performance is fully compatible with the previous test beam measurements. This demonstrates that the chamber behavior can be fully characterized using cosmic rays. Furthermore, we show that cosmic rays are as effective as collimated beams in the measurement of the wire misalignment and the layer shifts.

So far, the overall quality of the chambers built at Legnaro is satisfactory, with all parameters within the established tolerances. All the chamber features are well reproduced from chamber to chamber, as shown by fig. 24 for the electronic noise, by fig. 25 for the average SL efficiency, and by table 2 and figs. 26 and 27 for the MT resolution. The SL efficiency is always larger than 98%.

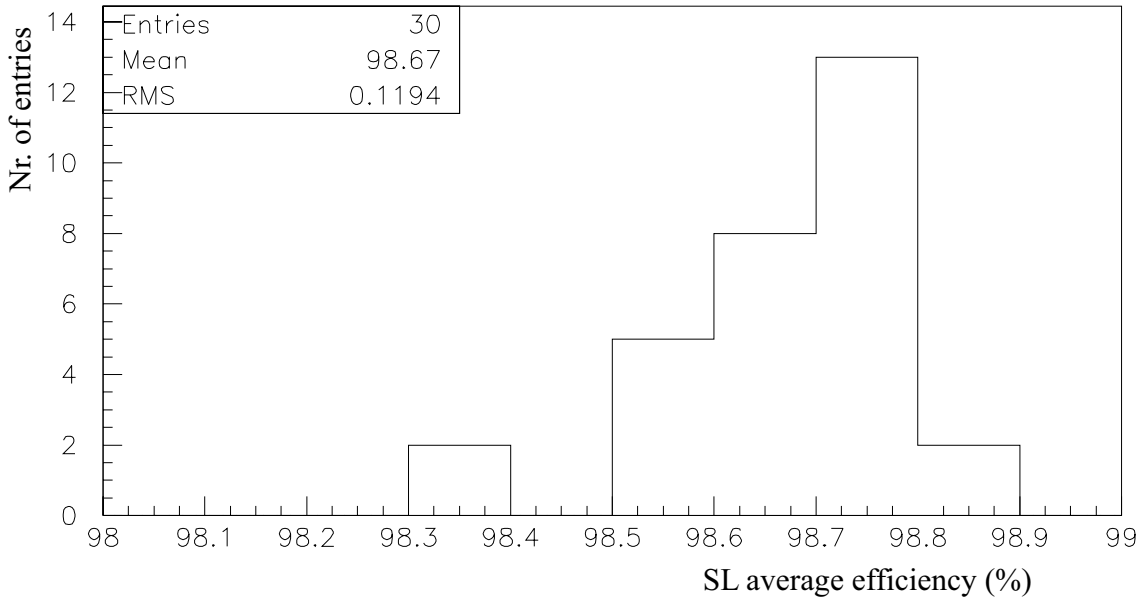

Figure 25: Distribution of the average SL efficiency for the first 11 MB3 chambers built at Legnaro.

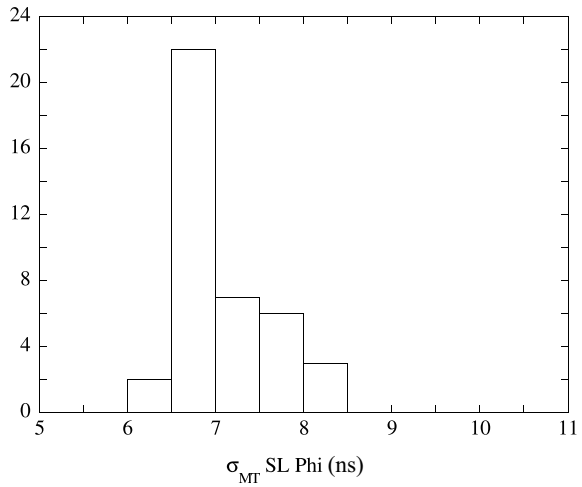

Figure 26: Distribution of the MT resolution (trigger resolution not subtracted) for all Φ SLs built at Legnaro. The resolutions of MT_1 and MT_2 are plotted together.

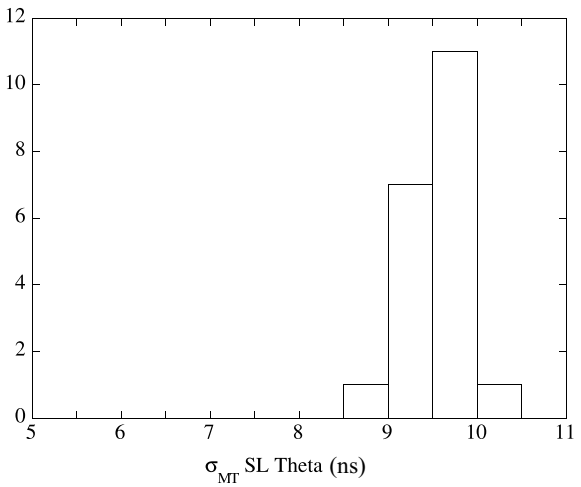

Figure 27: Distribution of the MT resolution (trigger resolution not subtracted) for all Θ SLs built at Legnaro. The resolutions of MT_1 and MT_2 are plotted together.

7 Acknowledgments

The measurements would not have been possible without the work of the DAQ group composed of M. Bellato, S. Ventura (INFN Padova) and L. Berti, M. Biasotto, E. Ferro, M. Gulmini, G. Maron, N. Toniolo, L. Zangrando (INFN Legnaro).

The authors acknowledge the skillful work of the technicians who assembled the MB3 chambers: A. Colombo, A. Griggio, M. Menorello, L. Modenese, U. Moschin, R. Pedrotta, G. Rampazzo (INFN Padova), F. Zatti (Padova University) and M. Boldini, M. Buldrini, V. Cafaro, V.‘Giordano, L. Maselli, S. Zagato (INFN Bologna), and the personnel of the technical office and the mechanical workshop of INFN Padova.

References

[1] CMS collaboration, *Muon Project Technical Design Report*, CERN LHCC97-32.

[2] F. Gasparini et al., *Nucl. Instrum. and Meth.* A 336 (1993), 91-97.

[3] F. Gasparini et al., *Changes in the design of the CMS muon barrel drift chambers*, CMS IN 1999/005.

[4] M. Bellato et al., in preparation.

[5] CMS collaboration, *Level-1 Trigger Technical Design Report*, CERN LHCC 2000-038.

[6] E. Conti et al., *Experimental test of the Q2 drift tube prototype chamber for the CMS muon barrel*, CMS Note 1997/019;

E. Conti, *Measurement of the wire gain of cells of the barrel muon drift chambers*, CMS Note 2002/002.

[7] S. Bethke et al., *Performance and mechanical tolerances achieved with a full size prototype of a CMS barrel muon drift tubes chamber*, CMS Note 1998/064.

[8] M. Aguilar-Benitez et al., *Nucl. Instrum. and Meth.* A 480 (2002), 658-669.

[9] M. Cerrada et al., *Results from the analysis of the test beam data taken with the barrel muon DT prototype Q4*, CMS Note 2001/041.

[10] M. Cerrada et al., *Test beam analysis of the first CMS MB2 drift tube muon chamber*, CMS Note 2003/007.

[11] M. Cavicchi et al., *Properties and performance of a front-end ASIC prototype for the readout of the CMS barrel muon drift tubes chambers*, CMS Note 1999/033;

[12] M. Bellato et al., *The validation system for the barrel muon chambers at LNL. Part 2: the cosmic set-up*, in preparation.

F. Gonella, M. Pegoraro, *"The MAD", a full custom ASIC for the CMS barrel muon chambers front-end electronics*, Proceedings of the VII workshop on electronics for LHC experiments, CERN LHCC 2001-034, 204-208.

[13] M. Passaseo et al., *Nucl. Instrum. and Meth.* A 367 (1995), 418-421.

[14] A. Cavestro et al., *Nucl. Instrum. and Meth.* A 305 (1991), 488-491.

[15] F. Sauli, *Principles of operation of multiwire proportional and drift chambers*, CERN 77-09 (1977).

[16] S. Paoletti, *A study of the CMS Q4 prototype chamber for different beam position along the wires*, CMS IN 2000/021.

[17] F. Gonella, private communication.

[18] J. F. de Troconiz, *Calibration and alignment procedures at the 2001 testbeam analysis*, CMS IN 2003/020.